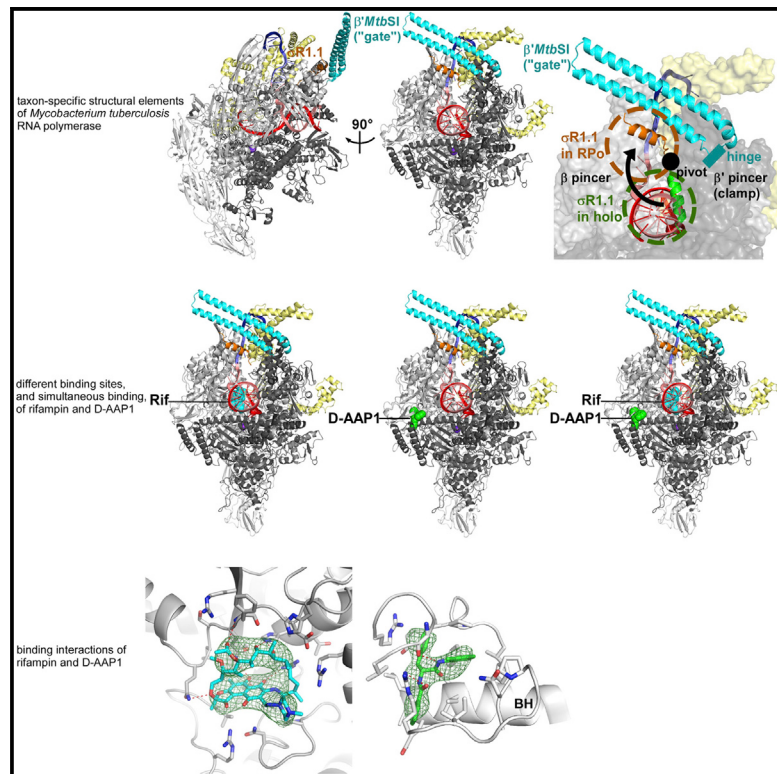


Molecular Cell

Structural Basis of *Mycobacterium tuberculosis* Transcription and Transcription Inhibition

Graphical Abstract



Authors

Wei Lin, Soma Mandal,
David Degen, ..., Kalyan Das,
Eddy Arnold, Richard H. Ebright

Correspondence

ebright@waksman.rutgers.edu

In Brief

Lin et al. report crystal structures of *Mycobacterium tuberculosis* RNA polymerase, alone and in complex with the antituberculosis compounds rifampin and D-AAP1. D-AAP1 interacts with a different binding site than rifampin, exhibits no cross-resistance with rifampin, functions additively when co-administered with rifampin, and suppresses resistance emergence when co-administered with rifampin.

Highlights

- Crystal structures of *Mycobacterium tuberculosis* RNA polymerase (*Mtb* RNAP)
- Crystal structures of *Mtb* RNAP in complex with antituberculosis drug rifampin
- Crystal structures of *Mtb* RNAP in complex with new antituberculosis compound D-AAP1
- Different binding sites and simultaneous binding of rifampin and D-AAP1

Structural Basis of *Mycobacterium tuberculosis* Transcription and Transcription Inhibition

Wei Lin,^{1,4} Soma Mandal,^{1,4} David Degen,¹ Yu Liu,¹ Yon W. Ebright,¹ Shengjian Li,¹ Yu Feng,¹ Yu Zhang,^{1,5} Sukhendu Mandal,¹ Yi Jiang,¹ Shuang Liu,¹ Matthew Gigliotti,¹ Meliza Talaue,² Nancy Connell,² Kalyan Das,^{3,6} Eddy Arnold,³ and Richard H. Ebright^{1,7,*}

¹Waksman Institute and Department of Chemistry and Chemical Biology, Rutgers University, Piscataway, NJ 08854, USA

²Center for Biodefense and Department of Medicine, New Jersey Medical School, Rutgers University, Newark, NJ 07101, USA

³Center for Advanced Biotechnology and Medicine and Department of Chemistry and Chemical Biology, Rutgers University, Piscataway, NJ 08854, USA

⁴Co-first author

⁵Present address: Shanghai Institute for Plant Physiology and Ecology, Chinese Academy of Sciences, Shanghai 200032, China

⁶Present address: Rega Institute and Department of Microbiology and Immunology, KU Leuven, 3000 Leuven, Belgium

⁷Lead Contact

*Correspondence: ebright@waksman.rutgers.edu

<http://dx.doi.org/10.1016/j.molcel.2017.03.001>

SUMMARY

Mycobacterium tuberculosis (*Mtb*) is the causative agent of tuberculosis, which kills 1.8 million annually. *Mtb* RNA polymerase (RNAP) is the target of the first-line antituberculosis drug rifampin (Rif). We report crystal structures of *Mtb* RNAP, alone and in complex with Rif, at 3.8–4.4 Å resolution. The results identify an *Mtb*-specific structural module of *Mtb* RNAP and establish that Rif functions by a steric-occlusion mechanism that prevents extension of RNA. We also report non-Rif-related compounds—N α -aryloyl-N-aryl-phenylalaninamides (AAPs)—that potently and selectively inhibit *Mtb* RNAP and *Mtb* growth, and we report crystal structures of *Mtb* RNAP in complex with AAPs. AAPs bind to a different site on *Mtb* RNAP than Rif, exhibit no cross-resistance with Rif, function additively when co-administered with Rif, and suppress resistance emergence when co-administered with Rif.

INTRODUCTION

Rifampin (Rif) is the cornerstone of current antituberculosis therapy (World Health Organization, 2016; Rothstein, 2016; Aristoff et al., 2010). The emergence and spread of Rif-resistant *Mycobacterium tuberculosis* (*Mtb*) is an urgent public health crisis (0.6 million new cases annually; World Health Organization, 2016). Rif resistance in *Mtb* arises from substitution of residues of the binding site for Rif on its molecular target, *Mtb* RNA polymerase (RNAP) (Rothstein, 2016; Aristoff et al., 2010). Intensive efforts are underway to identify Rif derivatives that are unaffected by substitutions in the Rif binding site and to identify novel, non-Rif-related RNAP inhibitors that function through binding sites on RNAP that do not overlap the Rif binding site and thus are unaffected by substitutions in the Rif binding site

(Aristoff et al., 2010; Lee and Borukhov, 2016). However, these efforts have been hampered by the unavailability of structural information for *Mtb* RNAP or a closely related bacterial RNAP. Crystal structures of bacterial RNAP hitherto have been available only for *Thermus aquaticus* (*Taq*), *Thermus thermophilus* (*Tth*), and *Escherichia coli* (*Eco*) RNAP, which have \leq 40% sequence identity with *Mtb* RNAP (Murakami, 2015), although a paper reporting a structure of *Mycobacterium smegmatis* RNAP recently has appeared (Hubin et al., 2017).

Here, we report a series of crystal structures of *Mtb* RNAP transcription initiation complexes at 3.8–4.4 Å resolution. We report structures of *Mtb* RNAP transcription initiation complexes alone, in complex with Rif, in complex with a non-Rif-related RNAP inhibitor, and in complex with both Rif and a non-Rif-related RNAP inhibitor.

RESULTS AND DISCUSSION

To determine crystal structures of *Mtb* RNAP transcription initiation complexes, we used a strategy analogous to the strategy used previously to determine structures of *Tth* RNAP transcription initiation complexes (Zhang et al., 2012), i.e., crystallization of *Mtb* RNAP σ^A holoenzyme in complex with a synthetic nucleic-acid scaffold that mimics the single-stranded DNA (ssDNA) transcription bubble and downstream double-stranded DNA (dsDNA) of a catalytically competent RNAP promoter open complex (RPO) or with the same synthetic nucleic-acid scaffold in the presence of synthetic RNA oligomers corresponding to 2-, 3-, and 4-nt RNA products (RNAP-promoter initial transcribing complexes, RPItc2, RPItc3, and RPItc4) (Table 1; Figure 1).

The resulting structures of *Mtb* RPO and RPItc are similar to previously reported structures of *Tth* RPO and RPItc (Zhang et al., 2012) in overall structural organization; in sequence-specific interactions between RNAP holoenzyme and promoter –10, discriminator, and core recognition elements; and in sequence-independent interactions between RNAP holoenzyme and template-strand ssDNA and downstream dsDNA (Figures 1B, 2, S1, and S2).

Table 1. Structure Data Collection and Refinement Statistics

Complex	<i>Mtb</i> RPo	<i>Mtb</i> RPo + 2-nt RNA	<i>Mtb</i> RPo + 3-nt RNA	<i>Mtb</i> RPo + 4-nt RNA	<i>Mtb</i> RPo + Rif	<i>Mtb</i> RPo + Rif + 2-nt RNA	<i>Mtb</i> RPo + Rif + 3-nt RNA	<i>Mtb</i> RPo + Rif + 4-nt RNA	<i>Mtb</i> RPo + D-AAP1	<i>Mtb</i> RPo + D-IX336	<i>Mtb</i> RPo + Rif + D-AAP1	<i>Mtb</i> Se-β'MtbsI
PDB code	PDB: 5UHA	PDB: 5UH9	PDB: 5UH5	PDB: 5UH8	PDB: 5UHB	PDB: 5UH6	PDB: 5UHC	PDB: 5UHD	PDB: 5UHE	PDB: 5UHF	PDB: 5UHG	PDB: 5UH7
Data collection source	APS 19-ID	APS 19-ID										
Data Collection												
Space group	P2 ₁ 2 ₁ 2 ₁	P2 ₁										
Cell Dimensions												
a, b, c	150.2, 163.5, 195.6 Å	154.5, 164.6, 201.9 Å	150.3, 163.6, 195.5 Å	152.0, 163.7, 197.8 Å	154.4, 164.2, 200.2 Å	153.2, 164.9, 199.9 Å	150.1, 167.4, 195.2 Å	152.1, 163.1, 197.9 Å	151.5, 162.1, 195.7 Å	152.4, 163.5, 197.4 Å	151.4, 162.1, 194.3 Å	40.8, 97.5, 53.7 Å
α, β, γ	90.0°, 90.0°, 90.0°	90.0°, 93.3°, 90.0°										
Resolution	50.0–3.9 Å (4.0–3.9 Å)	50.0–4.4 Å (4.6–4.4 Å)	50.0–3.8 Å (3.9–3.8 Å)	50.0–4.2 Å (4.3–4.2 Å)	50.0–4.2 Å (4.4–4.2 Å)	50.0–3.8 Å (3.9–3.8 Å)	50.0–4.0 Å (4.1–4.0 Å)	50.0–4.0 Å (4.2–4.0 Å)	50.0–4.3 Å (4.5–4.3 Å)	50.0–4.0 Å (4.1–4.0 Å)	50.0–2.2 Å (2.3–2.2 Å)	
Number of unique reflections	44,080	31,061	50,207	35,874	33,869	47,440	48,275	41,864	39,805	32,776	41,653	21,229
R _{merge}	0.219 (0.837)	0.191 (0.542)	0.175 (0.710)	0.172 (0.669)	0.066 (0.543)	0.134 (0.800)	0.169 (0.903)	0.096 (0.875)	0.216 (0.716)	0.203 (0.913)	0.243 (0.801)	0.075 (0.508)
R _{meas}	0.226 (0.877)	0.202 (0.624)	0.184 (0.764)	0.183 (0.740)	0.072 (0.609)	0.142 (0.901)	0.178 (0.965)	0.101 (0.931)	0.230 (0.781)	0.212 (0.956)	0.258 (0.862)	0.086 (0.593)
R _{pim}	0.057 (0.253)	0.062 (0.300)	0.055 (0.273)	0.060 (0.299)	0.028 (0.270)	0.046 (0.401)	0.053 (0.331)	0.030 (0.312)	0.076 (0.301)	0.065 (0.428)	0.087 (0.313)	0.040 (0.302)
CC _{1/2} (highest resolution shell)	0.422	0.539	0.471	0.489	0.697	0.432	0.343	0.413	0.524	0.632	0.490	0.791
I/σI	10.1 (1.5)	7.6 (1.8)	13 (2.0)	8.8 (1.4)	20.2 (2.0)	14.2 (1.6)	11.0 (2.0)	23.5 (1.9)	8.0 (1.9)	10.3 (1.3)	8.1 (2.1)	16.5 (5.4)
Completeness	99.2% (99.4%)	93.3% (81.7%)	99.7% (99.3%)	96.1% (82.6%)	97.0% (89.0%)	97.7% (92.6%)	97.4% (94.3%)	99.8% (98.6%)	99.2% (98.6%)	99.0% (96.7%)	99.8% (92.8%)	99.4% (99.9%)
Redundancy	15.0 (8.2)	7.6 (3.4)	10.4 (7.4)	7.8 (4.4)	5.9 (4.5)	7.5 (4.3)	9.9 (7.5)	11.1 (8.2)	7.4 (6.0)	12.1 (8.5)	8.3 (7.4)	4.3 (3.5)
Refinement												
Resolution	48.9–3.9 Å	49.9–4.4 Å	49.6–3.8 Å	48.6–4.2 Å	49.8–4.3 Å	50.0–3.8 Å	48.8–3.8 Å	49.5–4.0 Å	49.3–4.0 Å	48.5–4.3 Å	49.2–4.0 Å	36.1–2.2 Å
Number of unique reflections	34,564	28,534	46,464	29,908	29,562	39,783	43,854	38,089	34,622	28,581	39,399	18,943
Number of test reflections	1,988	1,993	1,997	1,987	2,005	1,996	2,000	1,990	2,007	3,135	2,014	1,835
R _{work} /R _{free}	0.22/0.27 (0.25/0.33)	0.28/0.33 (0.30/0.34)	0.19/0.24 (0.24/0.30)	0.20/0.25 (0.21/0.25)	0.21/0.26 (0.23/0.26)	0.21/0.26 (0.25/0.31)	0.20/0.26 (0.27/0.32)	0.21/0.26 (0.26/0.32)	0.21/0.26 (0.25/0.28)	0.20/0.26 (0.24/0.30)	0.22/0.26 (0.28/0.34)	0.22/0.25 (0.30/0.34)

(Continued on next page)

Table 1. Continued

Complex	Mtb RPo	Mtb RPo + 2-nt RNA	Mtb RPo + 3-nt RNA	Mtb RPo + 4-nt RNA	Mtb RPo + Rif	Mtb RPo + Rif + 2-nt RNA	Mtb RPo + Rif + 3-nt RNA	Mtb RPo + Rif + 4-nt RNA	Mtb RPo + D-AAPI	Mtb RPo + D-IK336	Mtb RPo + Rif + D-AAPI	Mtb Se-β'MtbSI
Number of Atoms												
Protein	25,995	26,033	26,078	26,098	25,994	26,033	26,056	25,973	25,952	25,973	25,964	2,153
Ligand/ion	3	3	3	3	62	62	62	62	30	29	89	N/A
Water	N/A	N/A	N/A	N/A	N/A	N/A	N/A	N/A	N/A	N/A	N/A	45
Root-Mean-Square (RMS) Deviations												
Bond lengths	0.005 Å	0.004 Å	0.004 Å	0.004 Å	0.003 Å	0.004 Å	0.004 Å	0.004 Å	0.005 Å	0.003 Å	0.003 Å	0.010 Å
Bond angles	0.793°	0.681°	0.763°	0.692°	0.709°	0.730°	0.733°	0.737°	0.804°	0.701°	0.702°	1.170°
MolProbity Statistics												
Clash score	8.5	8.0	8.9	7.6	7.0	7.1	7.1	7.5	9.4	8.0	7.4	5.4
Rotamer outliers	1.8%	1.4%	2.2%	1.4%	1.3%	1.6%	1.7%	1.6%	2.1%	2.2%	1.7%	0.0%
Cβ outliers	0%	0%	0%	0%	0%	0%	0%	0%	0%	0%	0%	0%
Ramachandran Plot												
Favored	93.3%	94.2%	93.5%	94.2%	94.5%	94.0%	94.0%	94.1%	93.9%	93.2%	94.5%	98.8%
Outliers	0.7%	0.5%	0.7%	0.6%	0.5%	0.5%	0.5%	0.5%	0.5%	0.5%	0.5%	0.0%

The highest resolution shells are in parentheses.

The structures reveal two distinctive features.

First, the structures reveal the conformation and interactions of an ~100-residue taxon-specific sequence insertion present in the β' subunit of RNAP from mycobacterial and closely related acinetobacterial taxa (β'MtbSI; β'In1 in Lane and Darst, 2010; β' residues 140–229, Figures 3A–3C). The structures of Mtb RPo and RPItc show that β'MtbSI folds as an extraordinarily long (~70-Å) α-helical coiled-coil (Figures 3A and 3B), and a structure at 2.2-Å resolution of an isolated protein fragment corresponding to β'MtbSI shows a superimposable conformation and thus shows that β'MtbSI folds independently (Figure 3B; Table 1). In the structures of Mtb RPo and RPItc, the β'MtbSI coiled-coil emerges from the RNAP clamp module and extends across the RNAP active-center cleft (Figures 3A and 3C). We infer that the β'MtbSI coiled-coil serves as a “gate” that helps trap and secure DNA within the active-center cleft and that presumably must open, rotating about a “hinge” formed by the short unstructured segments connecting β'MtbSI to the remainder of β', to allow DNA to enter the active-center cleft (Figure 3C). Consistent with the inference from the structures that β'MtbSI helps trap and secure DNA within the active-center cleft, deletion of β'MtbSI strongly reduces the stability of Mtb RPo (10-fold defect; Figure 3D). We suggest that the taxon-specific sequence insertion β'MtbSI, like the taxon-specific stabilizing general transcription factors CarD and RpbA (Davis et al., 2015; Hubin et al., 2017), is a mycobacterial adaptation that helps overcome the unusual intrinsic instability of the mycobacterial RPo (Davis et al., 2015).

Second, the structures provide information about the position of σR1.1, a σ module that, based on fluorescence resonance energy transfer (FRET) data, occupies the dsDNA binding site within the RNAP active-center cleft in RNAP holoenzyme but is displaced from the dsDNA binding site upon formation of RPo (Mekler et al., 2002; Figures 3A and 3C). A structure of *Eco* RNAP holoenzyme shows that σR1.1 occupies the dsDNA binding site in RNAP holoenzyme (Bae et al., 2013), consistent with the FRET data (Mekler et al., 2002), but previous structures of bacterial RPo and RPItc have not resolved σR1.1 (Zhang et al., 2012). The structures of Mtb RPo and RPItc show clear, unambiguous electron density for one α helix of σR1.1, the α helix that connects σR1.1 to the remainder of σ (H4; numbered as in Zhang et al., 2012; Figures 3A and 3C). Strikingly, whereas in *Eco* RNAP holoenzyme, H4 is oriented perpendicular to the floor of the dsDNA binding site and occupies the dsDNA binding site (green in Figures 1B and S3A), in Mtb RPo and RPItc, H4 is rotated by ~100°, about a “pivot” formed by the short unstructured segment between σR1.1 and the remainder of σ, and is oriented essentially parallel to the floor of the dsDNA binding site, outside the dsDNA binding site in Mtb RPo and RPItc (orange in Figures 3C and S3A). The rotation of H4 in RPo and RPItc displaces the center of H4 by ~30 Å from its position in RNAP holoenzyme, consistent with the FRET data (Mekler et al., 2002), and positions H4 between β'MtbSI and dsDNA (Figures 3C and S3A). Assuming Mtb σR1.1 has approximately the same molecular volume as *Eco* σR1.1, σR1.1 in Mtb RPo and RPItc occupies essentially the entire space between β'MtbSI and dsDNA, potentially making a continuous chain of β'MtbSI-σR1.1-dsDNA interactions that close the active center and help trap and secure dsDNA in the active center (Figures 3C and S3B). Consistent

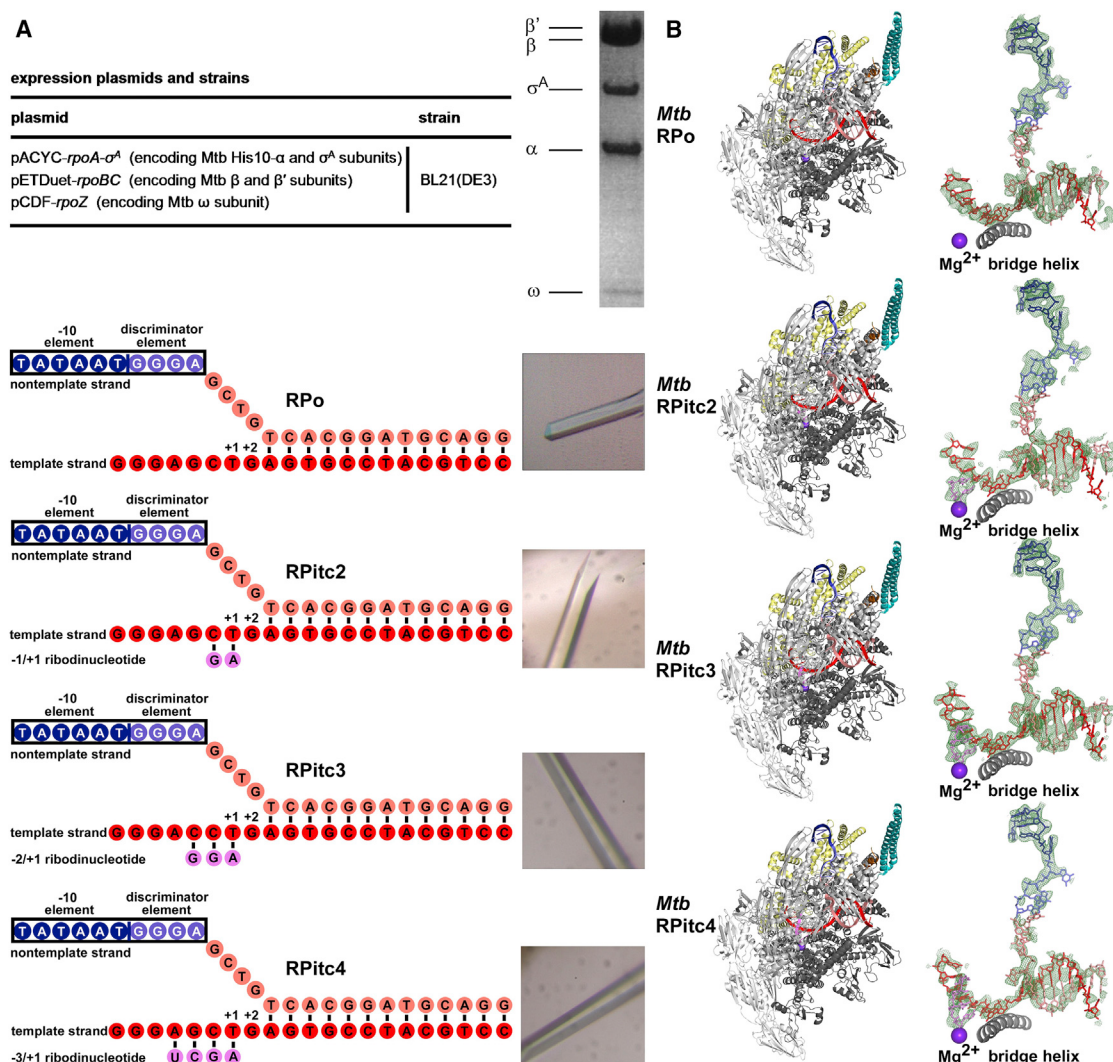


Figure 1. Structure Determination: *Mtb* RPo, *Mtb* RPitc2, *Mtb* RPitc3, and *Mtb* RPitc4

(A) Structure determination. Top left: plasmids and strain for production of *Mtb* RNAP σ^A holoenzyme in *E. coli* (Jacques et al., 2006; Banerjee et al., 2014). Top right: Coomassie-stained SDS-PAGE of *Mtb* RNAP σ^A holoenzyme produced in *E. coli*. Bottom: nucleic-acid scaffolds (left panels) and crystals (right panels).

(B) Overall structures and electron density. Left: overall structures. Gray, *Mtb* RNAP; yellow, *Mtb* σ^A ; blue, -10 element of DNA nontemplate strand; light blue, discriminator element of DNA nontemplate strand; pink, rest of DNA nontemplate strand; red, DNA template strand; cyan, taxon-specific sequence insertion $\beta'MtbSI$; orange, $\sigma R1.1 H4$; violet sphere, active-center Mg^{2+} . Right: electron density and model for nucleic acids.

with this inference, deletion of *Mtb* $\sigma R1.1$ strongly reduces the stability of *Mtb* RPo (5-fold defect), and deletion of both *Mtb* $\sigma R1.1$ and $\beta'MtbSI$ very strongly reduces the stability of RPo (>70-fold defect; Figure 3D). We suggest that the stabilizing effect of *Mtb* $\sigma R1.1$, functioning together with $\beta'MtbSI$, is a taxon-specific mycobacterial adaptation that further helps overcome the unusual intrinsic instability of mycobacterial RPo (Davis et al., 2015). We note that, in *Eco* RNAP, in contrast to *Mtb* RNAP, deletion of $\sigma R1.1$ does not reduce the stability of RPo (Vuthoori et al., 2001).

We determined a crystal structure of *Mtb* RPo in complex with Rif using analogous procedures (Figures 4A–4C; Table 1). The experimental electron density for Rif could be fitted in a manner

that placed the ansa ring of Rif in a ring-shaped density feature, placed the (4-methyl-1-piperazinyl)iminomethyl side chain of Rif in an adjoining tab-shaped density feature, and positioned Rif H-bond-forming atoms adjacent to RNAP complementary H-bond-forming atoms (Figures 4B and 4C). The resulting structure shows RNAP-Rif interactions similar to those in previously reported structures of *Taq* RNAP, *Tth* RNAP, and *Eco* RNAP in complex with rifamycins (Campbell et al., 2001; Artsimovitch et al., 2005; Molodtsov et al., 2013) but, in this case, with a Rif binding-site sequence from a bacterial species for which Rif is a clinically relevant antibacterial drug (Figures 4B and 4C). The structure shows direct H-bonded contacts between Rif and two of the three residues most frequently substituted in

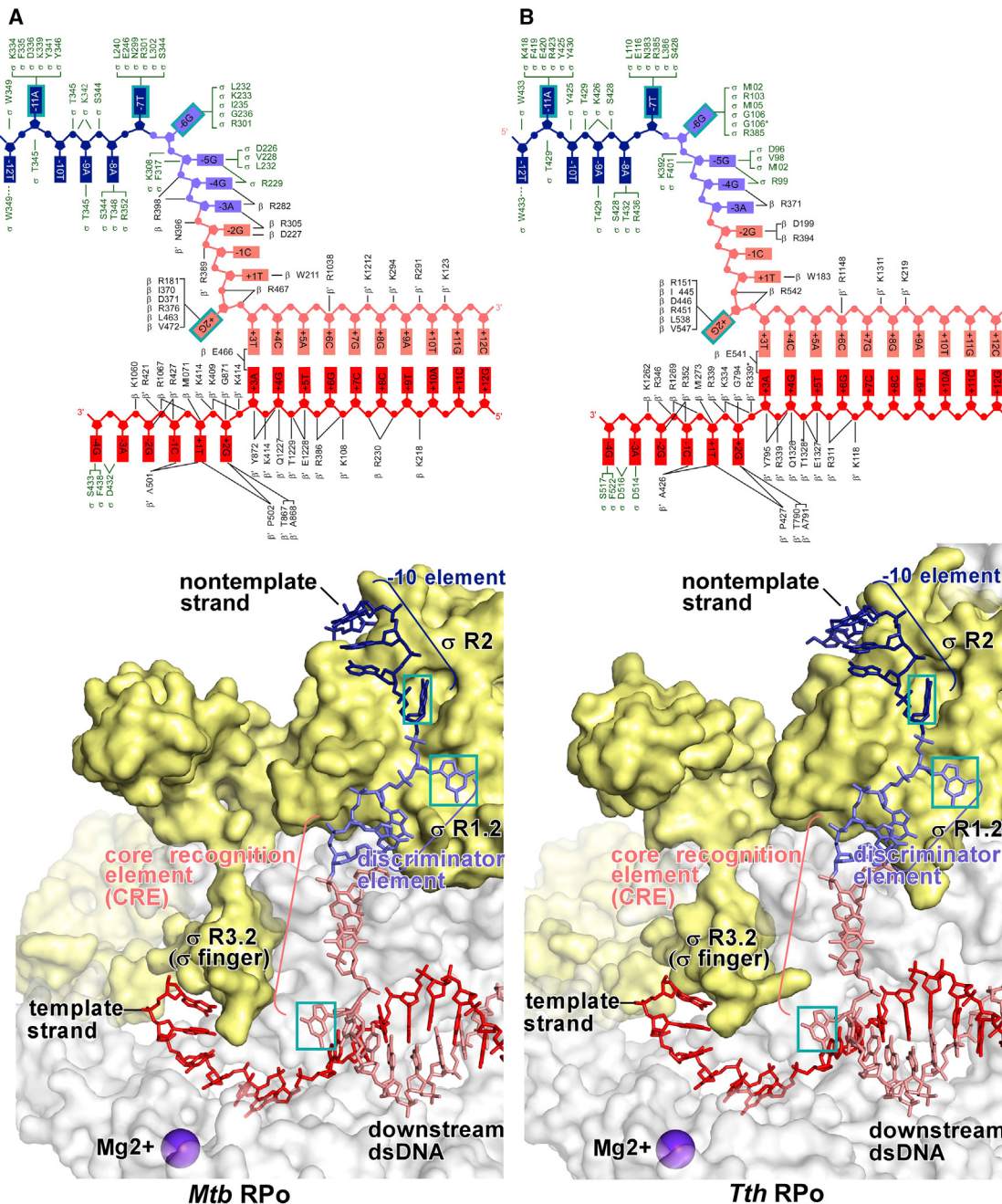


Figure 2. Conserved Features of *Mtb* RPo and *Tth* RPo

(A) Top: summary of protein-nucleic acid interactions in *Mtb* RPo. Black residue numbers and lines, interactions by *Mtb* RNAP; green residue numbers and lines, interactions by *Mtb* σ^A ; blue, -10 element of DNA nontemplate strand; light blue, discriminator element of DNA nontemplate strand; pink, rest of DNA nontemplate strand; red, DNA template strand; cyan boxes, bases unstacked and inserted into pockets. Residues are numbered as in *Mtb* RNAP. Bottom: interactions of *Mtb* RNAP and *Mtb* σ^A with transcription-bubble nontemplate strand, transcription-bubble template strand, and downstream dsDNA. Colors are as in Figure 1A.

(B) Top: summary of protein-nucleic acid interactions in *Tth* RPo (Zhang et al., 2012). Residues are numbered as in Eco RNAP. Bottom: interactions of *Tth* RNAP and *Tth* σ^A with transcription-bubble nontemplate strand, transcription-bubble template strand, and downstream dsDNA. Colors are as in (A).

See Figures S1 and S2.

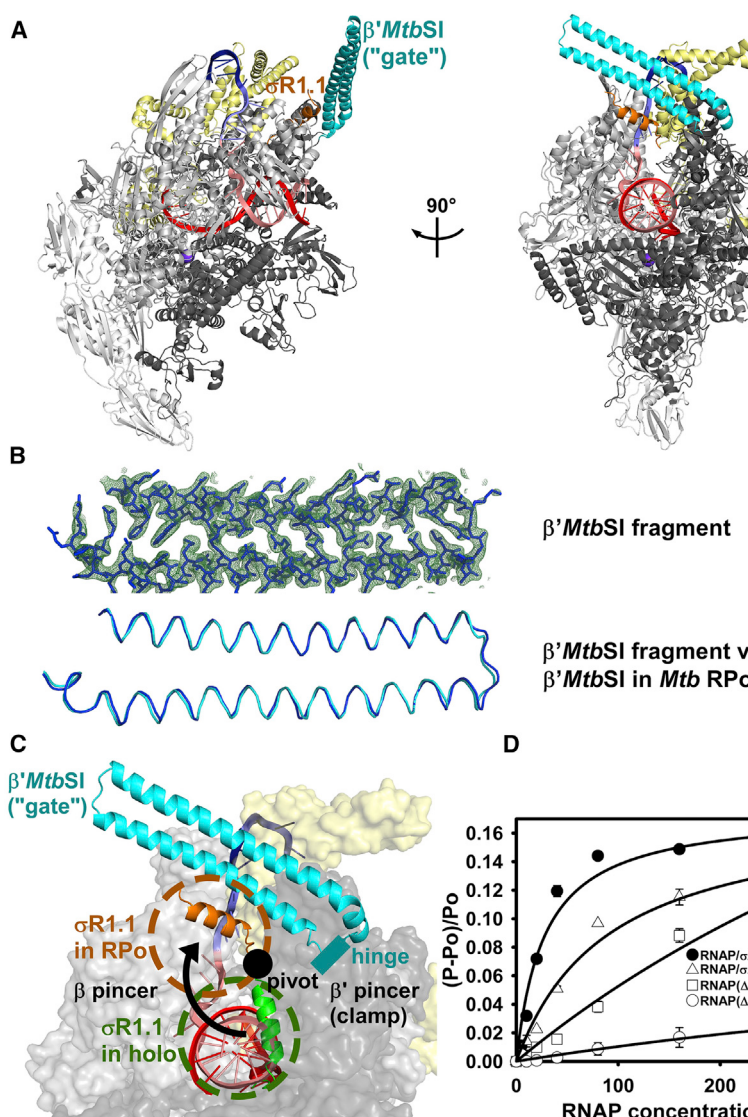


Figure 3. Distinctive Features of *Mtb* RPo: Taxon-Specific Sequence Insertion $\beta'MtbsI$ and $\sigma R1.1$

(A) Positions of taxon-specific sequence insertion $\beta'MtbsI$ (cyan) and $\sigma R1.1$ H4 (orange) in structure of *Mtb* RPo (two orthogonal views). Colors are as in Figure 1B.

(B) Structure of taxon-specific sequence insertion $\beta'MtbsI$. Top: electron density and model for $\beta'MtbsI$ from crystal structure of protein fragment *Mtb* $\beta'(141-229)$. Blue sticks, $\beta'MtbsI$ atoms; green mesh, $mF_o - F_c$ electron density omit map (contoured at 2.5σ). Bottom: superimposition of $\beta'MtbsI$ from structure of *Mtb* RPo (cyan) on $\beta'MtbsI$ from structure of *Mtb* $\beta'(141-229)$ (blue; 88 superimposed residues; rmsd = 0.65 \AA).

(C) Trapping of dsDNA in RNAP active-center cleft by $\beta'MtbsI$ and $\sigma R1.1$. Green and orange α helices, $\sigma R1.1$ in Eco RNA holoenzyme and *Mtb* RPo; green and orange dashed circles, approximate molecular volumes of $\sigma R1.1$ in Eco RNAP holoenzyme and *Mtb* RPo. Other colors are as in (A).

(D) Effects of deletion of $\beta'MtbsI$, $\sigma R1.1$, or both on stability of *Mtb* RPo. Error bars, mean \pm SEM. See Figure S3.

Rif-resistant *Mtb* clinical isolates (β H526 and S531) and direct van der Waals interactions between Rif and the third (β D516; Rothstein, 2016; Aristoff et al., 2010; Figures 4B and 4C).

A series of crystal structures of *Mtb* RPIC in complex with Rif were obtained by crystallizing a pre-formed *Mtb* RNAP-Rif complex with nucleic-acid scaffolds containing RNA oligomers corresponding to 2-, 3-, and 4-nt RNA products (Table 1). The results graphically demonstrate that Rif inhibits transcription through a “steric occlusion” mechanism that prevents extension of 2- to 3-nt RNA products to yield longer RNA products—a mechanism that previously had been proposed (Campbell et al., 2001; Mustaev et al., 1994; Feklistov et al., 2008) but had not been directly demonstrated and had been controversial (Artimovitch et al., 2005; Feklistov et al., 2008) (Figures 4D and 4E; Table 1). Thus, whereas in the absence of Rif, 2-, 3-, and 4-nt RNA products fully base pair to the DNA template strand (Figure 4D), in the presence of Rif, the 5' nucleotide of a 3-nt RNA is unpaired, unstacked, and rotated by $\sim 40^\circ$, due to steric clash with Rif (Figure 4E, second

and fourth panels), and a 4-nt RNA appears to be unable to interact stably with the complex (i.e., shows no density; Figure 4E, third panel). All the *Mtb* RPo-Rif and RPIC-Rif structures show clear, unambiguous electron density for the RNAP active-center catalytic Mg^{2+} , unlike the structure of *Tth* RNAP-Rif (Artimovitch et al., 2005) and inconsistent with the alternative, “allosteric” mechanism for Rif function proposed in Artimovitch et al. (2005) (Figures 4D and 4E).

By high-throughput screening of a library of 114,000 synthetic compounds

using a 384-well microplate-based fluorescence-detected assay of promoter-dependent transcription by *Mtb* RNAP σ^A holoenzyme (details to be provided elsewhere), we have identified a class of small-molecule inhibitors of *Mtb* RNAP: $N\alpha$ -aryl-N-aryl-phenylalaninamides (AAPs) (Figure 5A). The prototype of the class, D-AAP1, exhibits potent, selective, stereospecific activity against mycobacterial RNAP (potent inhibition of *Mtb* RNAP but poor inhibition of other bacterial RNAP and human RNAP I, II, and III; Figures 5A and S4A) and exhibits potent, selective, stereospecific activity against mycobacteria (potent activity against *Mtb*, *M. avium*, and *M. smegmatis* but poor activity against other bacterial and mammalian cells; Figures 5A and S4A).

A crystal structure of *Mtb* RPo in complex with D-AAP1, determined by soaking pre-formed crystals of *Mtb* RPo with D-AAP1, defines the binding site, orientation, and interactions of D-AAP1 (Figure 5B; Table 1). Synthesis of a D-AAP1 analog containing a carbon-to-selenium substitution, D-IX336, followed by crystal soaking, X-ray diffraction analysis, and

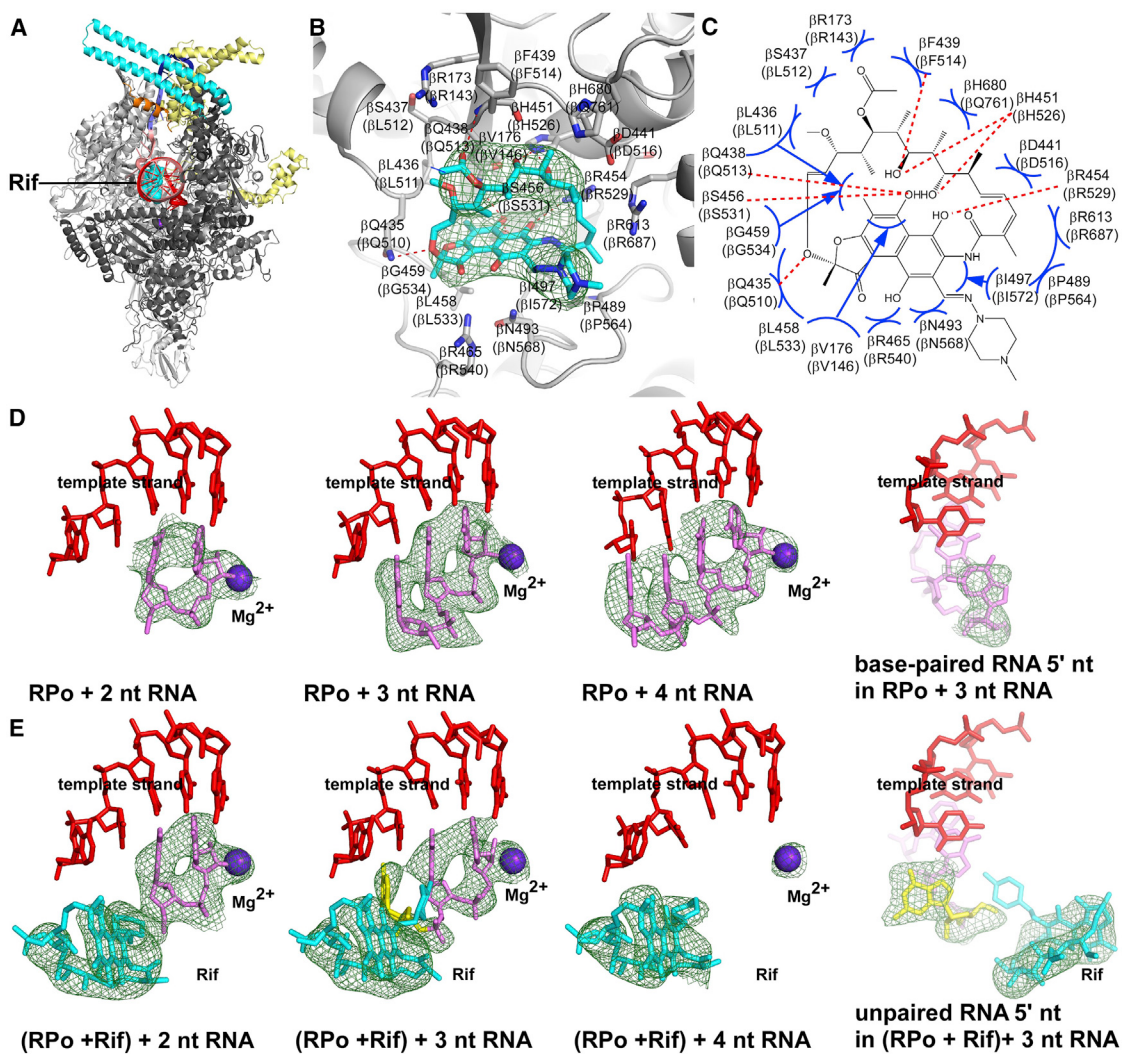


Figure 4. Structural Basis of *Mtb* RNAP Inhibition by Rif

(A) Overall structure of *Mtb* RNAP in complex with Rif. Cyan surface, Rif. Other colors are as in Figure 1B.

(B) *Mtb* RNAP-Rif interactions. Gray ribbons, RNAP backbone; gray and cyan sticks, RNAP and Rif carbon atoms; green mesh, mFo-Fc electron density omit map for Rif (contoured at 2.5σ); red and blue sticks, RNAP and Rif oxygen and nitrogen atoms. Residues are numbered as in *Mtb* RNAP and, in parentheses, as in *Eco* RNAP.

(C) Summary of *Mtb* RNAP-Rif interactions. Red dashed lines, H-bonds; blue arcs, van der Waals interactions.

(D and E) “Steric occlusion” mechanism for RNAP inhibition by Rif. Subpanels 1–3 of (D) show *Mtb* RNAP crystallized with nucleic acid scaffolds containing 2-, 3-, and 4-nt RNAs; subpanel 4 of (D) is an orthogonal view of subpanel 2, showing base pairing of RNA 5' nucleotide. Subpanels 1–3 of (E) show *Mtb* RNAP-Rif crystallized with nucleic acid scaffolds containing 2-, 3-, and 4-nt RNAs; subpanel 4 of (E) is an orthogonal view of subpanel 2, showing unpaired, unstacked, RNA 5' nucleotide. Cyan, Rif; green mesh, mFo-Fc electron density omit map for Rif, RNA, and catalytic Mg^{2+} (contoured at 2.5σ); red, DNA template strand; pink, RNA; yellow, unpaired, unstacked RNA 5' nucleotide; violet sphere, active-center catalytic Mg^{2+} .

selenium-anomalous-dispersion analysis confirms the identified binding site, orientations, and interactions (Figures 5A–5C and S4B; Table 1). The structures reveal that AAPs bind to *Mtb* RNAP at a binding site centered on the N terminus of the RNAP bridge helix (an α helix that bridges the RNAP active-center cleft and forms one wall of the RNAP active center; Figures 5B and 5C). The three aromatic rings of the AAP bind in three pocket-like subsites (Figures 5B–5D). Alanine substitution of a residue of the observed binding site results in AAP resistance, both for RNAP-inhibitory activity and for antibacterial activity,

confirming the functional importance of the observed interactions (Figure 5E). The structures enable rational, structure-based optimization of AAPs to improve potencies and properties. In particular, the structures show that the methyl group of ring “C” of the AAP projects into an unoccupied area with volume sufficient to accommodate at least six non-H atoms (Figures 5B–5D), allowing substitution of this position with diverse chemical functionality, including both linear and cyclic substituents. Lead-optimization efforts (to be described elsewhere) confirm the utility of the structures for structure-based lead optimization

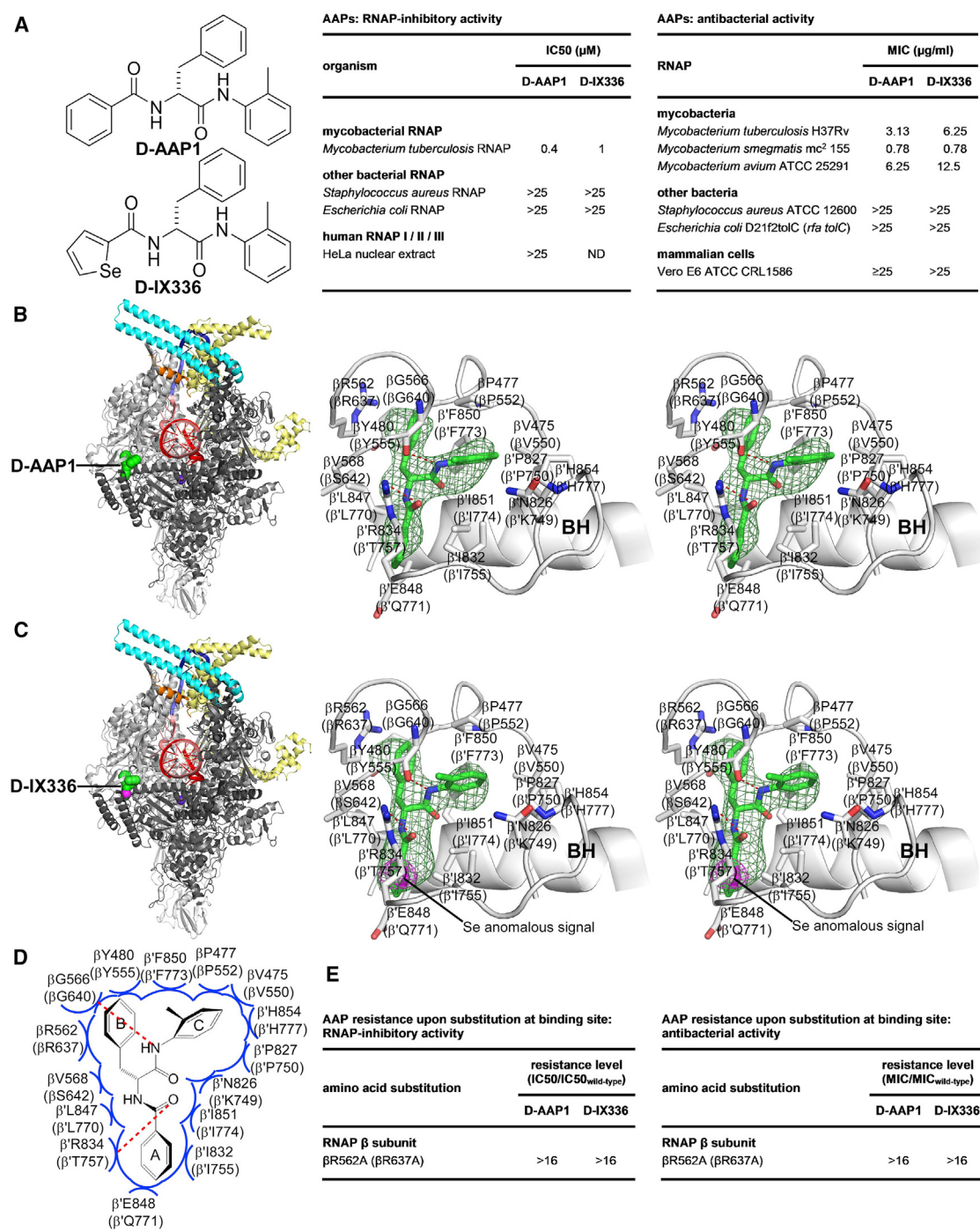


Figure 5. Structural Basis of *Mtb* RNAP Inhibition by AAPs

(A) Structures, RNAP-inhibitory activities, and antibacterial activities of D-AAP1 and selenium-containing analog D-IX336.

(B and C) Structures of *Mtb* RPo in complex with D-AAP1 (B) and D-IX336 (C), respectively (left panels, overall structures; right subpanels, stereoviews of *Mtb* RNAP-inhibitor interactions). Green surface, inhibitor; pink surface, selenium; green and pink sticks, inhibitor carbon and selenium atoms; pink mesh, selenium anomalous difference density (contoured at 4.5σ); BH, RNAP bridge helix. Other colors and labels are as in Figure 4B.

(D) Summary of *Mtb* RNAP-inhibitor interactions. Colors and labels are as in Figure 4C.

(E) Effects of Ala substitution of binding site residue.

See Figures S4–S6.

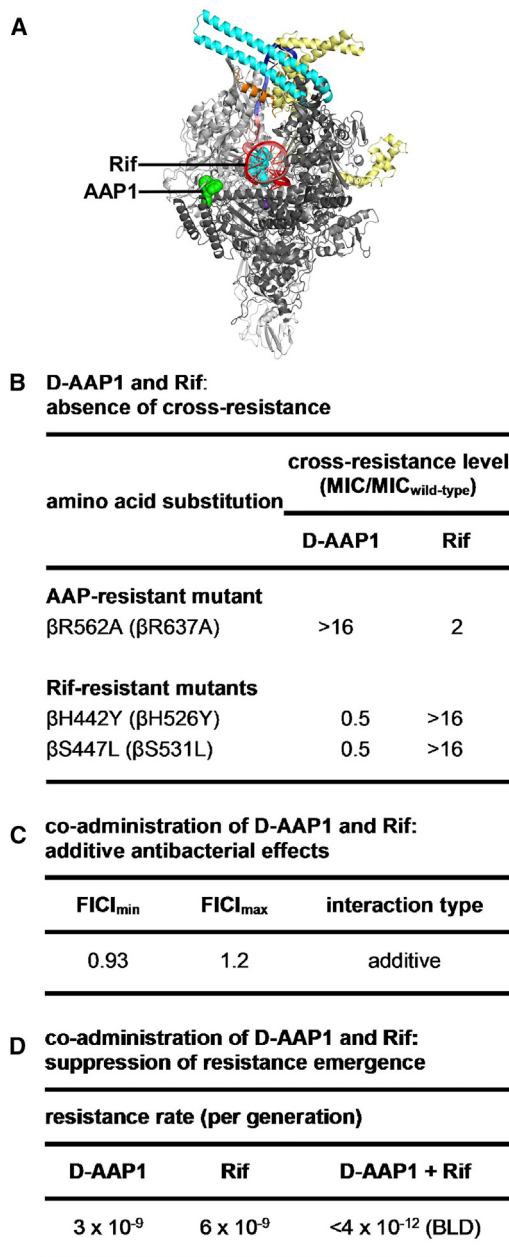


Figure 6. Additive Antibacterial Activity and Suppressed Resistance Emergence upon Co-administration of D-AAP1 and Rif

(A) Structure of *Mtb* RPo in complex with both D-AAP1 and Rif. Colors are as in Figures 4 and 5.
 (B) Absence of cross-resistance of D-AAP1 and Rif.
 (C) Additive antibacterial effects upon co-administration of D-AAP1 and Rif.
 (D) Suppressed resistance emergence upon co-administration of D-AAP1 and Rif. BLD, below limit of detection.

and, in particular, confirm the ability to improve potency and properties by substitution of the methyl group of ring C.

The structures in Figure 5 show that the binding site on RNAP for AAPs differs from, and does not overlap, the binding site on RNAP for Rif (Figures 4A, 5B, and 5C). The binding site on

RNAP for AAPs is similar in location to the binding site for CBRs, a class of compounds that inhibit Gram-negative bacterial RNAP but do not inhibit mycobacterial RNAP (Artimovitch et al., 2003; Feng et al., 2015; Bae et al., 2015; Figure S5). Thus, both AAPs (in *Mtb* RNAP) and CBRs (in Gram-negative RNAP) interact with the RNAP bridge-helix N terminus (Figures 5B–5D and S5). We infer that AAPs are mycobacteria-selective inhibitors that function through the bridge-helix N terminus target, and CBRs are Gram-negative-selective inhibitors that function through the bridge-helix N terminus. Comparison of structures of *Mtb* RNAP-AAP complexes and *Eco* RNAP-CBR complexes reveals the basis for the difference in selectivity, i.e., because of sequence differences, *Mtb* RNAP has a three-pocket site complementary to an AAP, with three rings, but *Eco* RNAP has a two-pocket site complementary to a CBR, with two rings (Figures S5 and S6). The crucial sequence differences apparently include β residue 642 and β' residues 757 and 771, which line or approach the pocket that is present, and accommodates AAP ring “A,” in *Mtb* RNAP, but is absent in *Eco* RNAP (residues numbered as in *Eco* RNAP; Figures S5 and S6). The binding-site residues for AAPs and CBRs are not conserved in human RNAP I, RNAP II, and RNAP III (Figure S6), consistent with, and accounting for, the observations that AAPs and CBRs do not inhibit human RNAP I, RNAP II, and RNAP III (Figure 5A; Feng et al., 2015). Based on the similarity in binding sites of AAPs and CBRs, AAPs most likely inhibit RNAP through a mechanism similar to that of CBRs, i.e., interference with bridge-helix conformational dynamics required for nucleotide addition (Feng et al., 2015; Bae et al., 2015).

A structure of *Mtb* RPo in complex with both D-AAP1 and Rif further confirms unequivocally that the AAP binding site differs from, and does not overlap, the Rif binding site and shows that an AAP and Rif can bind simultaneously to RNAP (Figure 6A; Table 1).

The absence of overlap between the AAP and Rif binding sites (Figure 6A) predicts that AAPs and Rif should not exhibit cross-resistance (because binding-site substitutions that interfere with binding of one compound should not affect binding of the other compound). Measurement of cross-resistance validates this prediction (Figure 6B). Thus, a substitution in the AAP binding site confers AAP resistance, but not Rif resistance, and substitutions in the Rif binding site confer Rif resistance, but not AAP resistance (Figure 6B).

The ability of AAPs and Rif to bind simultaneously to RNAP (Figure 6A) predicts that co-administration of an AAP and Rif should result in additive antibacterial activity (because each compound should bind to its respective site and contribute to inhibition through its respective mechanism of inhibition). Measurement of inhibitor-inhibitor interactions in checkerboard interaction assays yields a fractional inhibitory concentration index (FICI) indicative of additive interactions, validating this prediction (Figure 6C).

The absence of cross-resistance between AAPs and Rif (Figure 6B) together with the additive antibacterial activities of AAPs and Rif (Figure 6C) predict that co-administration of an AAP and Rif should suppress resistance emergence (because resistance to co-administered AAP and Rif should require a

rare double mutational hit inactivating two binding sites rather than a single mutational hit inactivating one binding site). Luria-Delbrück fluctuation assays assessing spontaneous resistance rates for D-AAP1, Rif, and co-administered D-AAP1 and Rif validate this prediction (Figure 6D). Co-administering D-AAP1 and Rif results in a ≥ 750 -fold reduction—to undetectable levels—in spontaneous resistance rates (Figure 6D).

The structures presented here provide a foundation for understanding *Mtb* RNAP structure-function, for structure-based design of improved Rif derivatives effective against Rif-resistant *Mtb*, and for structure-based discovery and development of non-Rif-related *Mtb* RNAP inhibitors effective against Rif-resistant *Mtb*. The non-Rif-related *Mtb* RNAP inhibitors presented here—AAPs—exhibit potent antimycobacterial activity, no cross-resistance with Rif, additive antimycobacterial activity when co-administered with Rif, and suppression of resistance emergence—to undetectable levels—when co-administered with Rif. As such, AAPs represent *exceptionally promising* lead compounds for development of new antituberculosis drugs.

STAR★METHODS

Detailed methods are provided in the online version of this paper and include the following:

● KEY RESOURCES TABLE

● CONTACT FOR REAGENT AND RESOURCE SHARING

● METHOD DETAILS

- N α -benzoyl-N-(2-methylphenyl)-D/L-phenylalaninamide (DL-AAP1)
- N α -benzoyl-N-(2-methylphenyl)-D-phenylalaninamide (D-AAP1)
- N α -benzoyl-N-(2-methylphenyl)-L-phenylalaninamide (L-AAP1)
- N α -selenophenoyl-N-(2-methylphenyl)-D-phenylalaninamide (D-IX336)
- *M. tuberculosis* σ^A
- *M. tuberculosis* β' MtbsI
- *M. tuberculosis* RNAP Core Enzyme
- *M. tuberculosis* σ^A Holoenzyme
- Oligonucleotides
- Nucleic-Acid Scaffolds
- RNAP-DNA Interaction Assays
- RNAP-Inhibitory Activities
- Growth-Inhibitory Activities
- Resistance and Cross-Resistance Assays
- Checkerboard Interaction Assays
- Resistance-Rate Assays
- Structure Determination: Assembly of Transcription Initiation Complexes
- Structure Determination: Crystallization, Cryo-cooling, and Crystal Soaking
- Structure Determination: Data Collection and Reduction
- Structure Determination: Structure Solution and Refinement

● QUANTITATION AND STATISTICAL ANALYSIS

SUPPLEMENTAL INFORMATION

Supplemental Information includes six figures and can be found with this article online at <http://dx.doi.org/10.1016/j.molcel.2017.03.001>.

AUTHOR CONTRIBUTIONS

Sukhendu Mandal, Y.J., and S. Liu developed co-expression systems and purification procedures for preparation of *Mtb* RNAP. W.L., Y.L., and Y.Z. purified *Mtb* RNAP, crystallized *Mtb* RNAP, and determined structures. W.L., Y.F., K.D., and E.A. refined structures. Soma Mandal, D.D., M.G., M.T., and N.C. performed biochemical and microbiological assays. R.H.E. designed studies, analyzed data, and wrote the manuscript.

ACKNOWLEDGMENTS

This work was supported by NIH grants GM041376 and AI109713-8681 and Global Alliance for TB Drug Development contracts to R.H.E. We thank the Argonne National Laboratory for beamline access; S. Rodrigue, J. Mukhopadhyay, and C. Sassetti for plasmids; and S. Diamond, E. Lucumi, G. Waters, Z. Ma, K. Taneko, C. Cooper, K. Mdluli, and N. Fotouhi for discussion. Soma Mandal, Y.W.E., S. Li, and R.H.E. have patent filings on AAPs.

Received: February 2, 2017

Revised: February 15, 2017

Accepted: February 28, 2017

Published: April 6, 2017

SUPPORTING CITATIONS

The following references appear in the Supplemental Information: Hein and Landick (2010); Jokerst et al. (1989); Sweetser et al. (1987); Weinzierl (2010).

REFERENCES

- Adams, P.D., Afonine, P.V., Bunkóczki, G., Chen, V.B., Davis, I.W., Echols, N., Headd, J.J., Hung, L.W., Kapral, G.J., Grosse-Kunstleve, R.W., et al. (2010). PHENIX: a comprehensive Python-based system for macromolecular structure solution. *Acta Crystallogr. D Biol. Crystallogr.* **66**, 213–221.
- Aristoff, P.A., Garcia, G.A., Kirchhoff, P.D., and Showalter, H.D. (2010). Rifamycins—obstacles and opportunities. *Tuberculosis (Edinb.)* **90**, 94–118.
- Artsimovitch, I., Chu, C., Lynch, A.S., and Landick, R. (2003). A new class of bacterial RNA polymerase inhibitor affects nucleotide addition. *Science* **302**, 650–654.
- Artsimovitch, I., Vassylyeva, M.N., Svetlov, D., Svetlov, V., Perederina, A., Igarashi, N., Matsugaki, N., Wakatsuki, S., Tahirov, T.H., and Vassylyev, D.G. (2005). Allosteric modulation of the RNA polymerase catalytic reaction is an essential component of transcription control by rifamycins. *Cell* **122**, 351–363.
- Bae, B., Davis, E., Brown, D., Campbell, E.A., Wigneshweraraj, S., and Darst, S.A. (2013). Phage T7 Gp2 inhibition of *Escherichia coli* RNA polymerase involves misappropriation of σ^{70} domain 1.1. *Proc. Natl. Acad. Sci. USA* **110**, 19772–19777.
- Bae, B., Nayak, D., Ray, A., Mustae, A., Landick, R., and Darst, S.A. (2015). CBR antimicrobials inhibit RNA polymerase via at least two bridge-helix cap-mediated effects on nucleotide addition. *Proc. Natl. Acad. Sci. USA* **112**, E4178–E4187.
- Banerjee, R., Rudra, P., Prajapati, R.K., Sengupta, S., and Mukhopadhyay, J. (2014). Optimization of recombinant *Mycobacterium tuberculosis* RNA polymerase expression and purification. *Tuberculosis (Edinb.)* **94**, 397–404.
- Campbell, E.A., Korzheva, N., Mustae, A., Murakami, K., Nair, S., Goldfarb, A., and Darst, S.A. (2001). Structural mechanism for rifampicin inhibition of bacterial RNA polymerase. *Cell* **104**, 901–912.
- CLSI/NCCLS (Clinical and Laboratory Standards Institute) (2009). Methods for Dilution Antimicrobial Susceptibility Tests for Bacteria that Grow Aerobically; Approved Standard, Eighth Edition (CLSI/NCCLS), CLIS Document M07-A8.

- CCP4 (Collaborative Computational Project, Number 4) (1994). The CCP4 suite: programs for protein crystallography. *Acta Crystallogr. D Biol. Crystallogr.* 50, 760–763.
- Collins, L., and Franzblau, S.G. (1997). Microplate alamar blue assay versus BACTEC 460 system for high-throughput screening of compounds against *Mycobacterium tuberculosis* and *Mycobacterium avium*. *Antimicrob. Agents Chemother.* 41, 1004–1009.
- Davis, E., Chen, J., Leon, K., Darst, S.A., and Campbell, E.A. (2015). Mycobacterial RNA polymerase forms unstable open promoter complexes that are stabilized by CarD. *Nucleic Acids Res.* 43, 433–445.
- Degen, D., Feng, Y., Zhang, Y., Ebright, K.Y., Ebright, Y.W., Gigliotti, M., Vahedian-Movahed, H., Mandal, S., Talaue, M., Connell, N., et al. (2014). Transcription inhibition by the depsipeptide antibiotic salinamide A. *eLife* 3, e02451.
- Emsley, P., Lohkamp, B., Scott, W.G., and Cowtan, K. (2010). Features and development of Coot. *Acta Crystallogr. D Biol. Crystallogr.* 66, 486–501.
- Feklistov, A., Mekler, V., Jiang, Q., Westblade, L.F., Irschik, H., Jansen, R., Mustaev, A., Darst, S.A., and Ebright, R.H. (2008). Rifamycins do not function by allosteric modulation of binding of Mg²⁺ to the RNA polymerase active center. *Proc. Natl. Acad. Sci. USA* 105, 14820–14825.
- Feng, Y., Degen, D., Wang, X., Gigliotti, M., Liu, S., Zhang, Y., Das, D., Michalchuk, T., Ebright, Y.W., Talaue, M., et al. (2015). Structural basis of transcription inhibition by CBR hydroxamides and CBR pyrazoles. *Structure* 23, 1470–1481.
- Fralick, J., and Burns-Keliher, L. (1994). Additive effect of tolC and rfa mutations on the hydrophobic barrier of the outer membrane of *Escherichia coli* K-12. *J. Bacteriol.* 176, 6404–6406.
- Hall, B.M., Ma, C.X., Liang, P., and Singh, K.K. (2009). Fluctuation analysis CalculatOR: a web tool for the determination of mutation rate using Luria-Delbrück fluctuation analysis. *Bioinformatics* 25, 1564–1565.
- Hein, P.P., and Landick, R. (2010). The bridge helix coordinates movements of modules in RNA polymerase. *BMC Biol.* 8, 141.
- Heyduk, T., Ma, Y., Tang, H., and Ebright, R.H. (1996). Fluorescence anisotropy: rapid, quantitative assay for protein-DNA and protein-protein interaction. *Methods Enzymol.* 274, 492–503.
- Horrevorts, A.M., Michel, M.F., and Kerrebijn, K.F. (1987). Antibiotic interaction: interpretation of fractional inhibitory and fractional bactericidal concentration indices. *Eur. J. Clin. Microbiol.* 6, 502–503.
- Hubin, E.A., Fay, A., Xu, C., Bean, J.M., Saecker, R.M., Glickman, M.S., Darst, S.A., and Campbell, E.A. (2017). Structure and function of the mycobacterial transcription initiation complex with the essential regulator RbpA. *eLife* 6, e22520.
- Jacques, J.F., Rodrigue, S., Brzezinski, R., and Gaudreau, L. (2006). A recombinant *Mycobacterium tuberculosis* *in vitro* transcription system. *FEMS Microbiol. Lett.* 255, 140–147.
- Jokerst, R.S., Weeks, J.R., Zehring, W.A., and Greenleaf, A.L. (1989). Analysis of the gene encoding the largest subunit of RNA polymerase II in *Drosophila*. *Mol. Gen. Genet.* 215, 266–275.
- Lane, W.J., and Darst, S.A. (2010). Molecular evolution of multisubunit RNA polymerases: sequence analysis. *J. Mol. Biol.* 395, 671–685.
- Lee, J., and Borukhov, S. (2016). Bacterial RNA polymerase-DNA interaction—the driving force of gene expression and the target for drug action. *Front. Mol. Biosci.* 3, 73.
- Ma, W.T., Vh. Sandri, G., and Sarkar, S. (1992). Analysis of the Luria-Delbrück distribution using discrete convolution powers. *J. Appl. Probab.* 29, 255–267.
- Mekler, V., Kortkhonja, E., Mukhopadhyay, J., Knight, J., Revyakin, A., Kapanidis, A.N., Niu, W., Ebright, Y.W., Levy, R., and Ebright, R.H. (2002). Structural organization of bacterial RNA polymerase holoenzyme and the RNA polymerase-promoter open complex. *Cell* 108, 599–614.
- Meletiadis, J., Pournaras, S., Roilides, E., and Walsh, T.J. (2010). Defining fractional inhibitory concentration index cutoffs for additive interactions based on self-drug additive combinations, Monte Carlo simulation analysis, and *in vitro* *in vivo* correlation data for antifungal drug combinations against *Aspergillus fumigatus*. *Antimicrob. Agents Chemother.* 54, 602–609.
- Molodtsov, V., Nawarathne, I.N., Scharf, N.T., Kirchhoff, P.D., Showalter, H.D., Garcia, G.A., and Murakami, K.S. (2013). X-ray crystal structures of the *Escherichia coli* RNA polymerase in complex with benzoxazinorifamycins. *J. Med. Chem.* 56, 4758–4763.
- Murakami, K.S. (2015). Structural biology of bacterial RNA polymerase. *Biomolecules* 5, 848–864.
- Murphy, K.C., Papavinasasundaram, K., and Sasetti, C.M. (2015). Mycobacterial recombineering. *Methods Mol. Biol.* 1285, 177–199.
- Mustaev, A., Zaychikov, E., Severinov, K., Kashlev, M., Polyakov, A., Nikiforov, V., and Goldfarb, A. (1994). Topology of the RNA polymerase active center probed by chimeric rifampicin-nucleotide compounds. *Proc. Natl. Acad. Sci. USA* 91, 12036–12040.
- Otwinowski, Z., and Minor, W. (1997). Processing of X-ray diffraction data collected in oscillation mode. *Methods Enzymol.* 276, 307–326.
- Rothstein, D.M. (2016). Rifamycins, alone and in combination. *Cold Spring Harb. Perspect. Med.* 6, a027011.
- Sarkar, S., Ma, W.T., and Sandri, G.H. (1992). On fluctuation analysis: a new, simple and efficient method for computing the expected number of mutants. *Genetica* 85, 173–179.
- Srivastava, A., Talaue, M., Liu, S., Degen, D., Ebright, R.Y., Sineva, E., Chakraborty, A., Druzhinin, S.Y., Chatterjee, S., Mukhopadhyay, J., et al. (2011). New target for inhibition of bacterial RNA polymerase: 'switch region'. *Curr. Opin. Microbiol.* 14, 532–543.
- Srivastava, A., Degen, D., Ebright, Y.W., and Ebright, R.H. (2012). Frequency, spectrum, and nonzero fitness costs of resistance to myxopyronin in *Staphylococcus aureus*. *Antimicrob. Agents Chemother.* 56, 6250–6255.
- Stewart, F.M., Gordon, D.M., and Levin, B.R. (1990). Fluctuation analysis: the probability distribution of the number of mutants under different conditions. *Genetics* 124, 175–185.
- Stols, L., Millard, C.S., Dementieva, I., and Donnelly, M.I. (2004). Production of selenomethionine-labeled proteins in two-liter plastic bottles for structure determination. *J. Struct. Funct. Genomics* 5, 95–102.
- Sweetser, D., Nonet, M., and Young, R.A. (1987). Prokaryotic and eukaryotic RNA polymerases have homologous core subunits. *Proc. Natl. Acad. Sci. USA* 84, 1192–1196.
- Vuthoori, S., Bowers, C.W., McCracken, A., Dombroski, A.J., and Hinton, D.M. (2001). Domain 1.1 of the sigma(70) subunit of *Escherichia coli* RNA polymerase modulates the formation of stable polymerase/promoter complexes. *J. Mol. Biol.* 309, 561–572.
- Weinzierl, R.O. (2010). The nucleotide addition cycle of RNA polymerase is controlled by two molecular hinges in the Bridge Helix domain. *BMC Biol.* 8, 134.
- White, R.L., Burgess, D.S., Manduru, M., and Bosso, J.A. (1996). Comparison of three different *in vitro* methods of detecting synergy: time-kill, checkerboard, and E test. *Antimicrob. Agents Chemother.* 40, 1914–1918.
- World Health Organization (2016). Global Tuberculosis Report 2016 (WHO).
- Zhang, Y., Feng, Y., Chatterjee, S., Tuske, S., Ho, M.X., Arnold, E., and Ebright, R.H. (2012). Structural basis of transcription initiation. *Science* 338, 1076–1080.
- Zhang, Y., Degen, D., Ho, M.X., Sineva, E., Ebright, K.Y., Ebright, Y.W., Mekler, V., Vahedian-Movahed, H., Feng, Y., Yin, R., et al. (2014). GE23077 binds to the RNA polymerase 'i' and 'i+1' sites and prevents the binding of initiating nucleotides. *eLife* 3, e02450.

STAR★METHODS

KEY RESOURCES TABLE

REAGENT or RESOURCE	SOURCE	IDENTIFIER
Bacterial and Virus Strains		
<i>Escherichia coli</i> BL21(DE3)	Thermo Fisher/Invitrogen	Cat# C600003
<i>Escherichia coli</i> D21f2tolC (<i>rfa tolC</i>)	Fralick and Burns-Keliher, 1994	N/A
<i>Mycobacterium avium</i>	ATCC	ATCC 25291
<i>Mycobacterium smegmatis</i> mc ² 155	ATCC	ATCC 700084
<i>Mycobacterium smegmatis</i> mc ² 155 (<i>rpoB</i> '637'A)	This paper	N/A
<i>Mycobacterium smegmatis</i> 19420	ATCC	ATCC 19420
<i>Mycobacterium smegmatis</i> 19420 (<i>rpoB</i> '526'Y)	This paper	N/A
<i>Mycobacterium smegmatis</i> 19420 (<i>rpoB</i> '531'L)	This paper	N/A
<i>Mycobacterium tuberculosis</i> H37Rv	ATCC	ATCC 27294
<i>Staphylococcus aureus</i>	ATCC	ATCC 12600
Chemicals, Peptides, and Recombinant Proteins		
rifampin	Sigma-Aldrich	Cat# R3501
N α -benzoyl-N-(2-methylphenyl)-D/L-phenylalaninamide	This paper	N/A
N α -benzoyl-N-(2-methylphenyl)-D-phenylalaninamide	This paper	N/A
N α -benzoyl-N-(2-methylphenyl)-L-phenylalaninamide	This paper	N/A
N α -selenophenoyl-N-(2-methylphenyl)-D-phenylalaninamide	This paper	N/A
D/L-benzoyl phenylalanine	Chem-Impex	Cat# 05630
D-benzoyl phenylalanine	Chem-Impex	Cat# 03124
L-benzoyl phenylalanine	Chem-Impex	Cat# 03123
N-Fmoc-D-phenylalanine	Chem-Impex	Cat# 02444
oxalyl chloride	Sigma-Aldrich	Cat# 221015-25G
selenophene-2-carboxylic acid	LabNetwork	Cat# AI94225034662
propane phosphonic acid anhydride	Sigma-Aldrich	Cat# 431303
kanamycin	Sigma-Aldrich	Cat# K4000-25G
IPTG	Gold Bio	Cat# I2481C50
Ni-NTA-agarose	QIAGEN	Cat# 30230
nuclease free water	Thermo Fisher/Ambion	Cat# AM9937
γ -{2'-(2-benzothiazoyl)-60-hydroxybenzothiazole}-ATP	Jena Biosciences	Cat# NU-1700
7H9 broth	BD Biosciences	Cat# 283810
BBL Seven H11 agar	BD Biosciences	Cat# 271310
Middlebrook ADC enrichment	BD Biosciences	Cat# 212352
(2R,3R)-(−)-2,3-butanediol	Sigma-Aldrich	Cat# 237639-5G
Critical Commercial Assays		
QuikChange lightning site-directed mutagenesis kit	Agilent	Cat# 210519
Wizard Classic 1 crystal screening solution kit	Emerald/Rigaku	Cat# 1009530
Wizard Classic 2 crystal screening solution kit	Emerald/Rigaku	Cat# 1009531
Wizard Classic 3 crystal screening solution kit	Emerald/Rigaku	Cat# 1009533
Wizard Classic 4 crystal screening solution kit	Emerald/Rigaku	Cat# 1009534
Wizard Cryo 1 crystal screening solution kit	Emerald/Rigaku	Cat# 1009536
Wizard Cryo 2 crystal screening solution kit	Emerald/Rigaku	Cat# 1009537
Crystal Screen Cryo crystal screening solution kit	Hampton Research	Cat# HR2-122
Crystal Screen 2 Cryo crystal screening solution kit	Hampton Research	Cat# HR2-121
Crystal Screen crystal screening solution kit	Hampton Research	Cat# HR2-110

(Continued on next page)

Continued

REAGENT or RESOURCE	SOURCE	IDENTIFIER
Crystal Screen 2 crystal screening solution kit	Hampton Research	Cat# HR2-112
Detergent Screen HT crystal screening solution kit	Hampton Research	Cat# HR2-406
Additive Screen HT crystal screening solution kit	Hampton Research	Cat# HR2-138
Index crystal screening solution kit	Hampton Research	Cat# HR2-144
Natrix crystal screening solution kit	Hampton Research	Cat# HR2-116
Natrix 2 crystal screening solution kit	Hampton Research	Cat# HR2-117
PEG/Ion crystal screening solution kit	Hampton Research	Cat# HR2-126
PEG/Ion 2 crystal screening solution kit	Hampton Research	Cat# HR2-098
PEGRx 1 crystal screening solution kit	Hampton Research	Cat# HR2-082
PEGRx 2 crystal screening solution kit	Hampton Research	Cat# HR2-084
SaltRx 1 crystal screening solution kit	Hampton Research	Cat# HR2-107
SaltRx 2 crystal screening solution kit	Hampton Research	Cat# HR2-109
NeXtal Protein Complex Suite crystal screening solution kit	QIAGEN	Cat# 130715
NeXtal Nucleix Suite crystal screening solution kit	QIAGEN	Cat# 130719
Deposited Data		
<i>Mtb</i> RPo	This paper	PDB: 5UHA
<i>Mtb</i> RPo + 2 nt RNA	This paper	PDB: 5UH9
<i>Mtb</i> RPo + 3 nt RNA	This paper	PDB: 5UH5
<i>Mtb</i> RPo + 4 nt RNA	This paper	PDB: 5UH8
<i>Mtb</i> RPo + Rif	This paper	PDB: 5UHB
<i>Mtb</i> RPo + Rif + 2 nt RNA	This paper	PDB: 5UH6
<i>Mtb</i> RPo + Rif + 3 nt RNA	This paper	PDB: 5UHC
<i>Mtb</i> RPo + Rif + 4 nt RNA	This paper	PDB: 5UHD
<i>Mtb</i> RPo + D-AAP1	This paper	PDB: 5UHE
<i>Mtb</i> RPo + D-IX336	This paper	PDB: 5UHF
<i>Mtb</i> RPo + Rif + D-AAP1	This paper	PDB: 5UHG
<i>Mtb</i> Se-β'MtbSI	This paper	PDB: 5UH7
Experimental Models: Cell Lines		
Vero E6	ATCC	CRL 1586
Oligonucleotides		
GpA	TriLink	Cat# O-31009
GpGpA	TriLink	N/A - custom
UpCpGpA	TriLink	N/A - custom
scaffold nontemplate strand for RPo, RPitc2, RPitc3, and RPitc4: 5'-TATAATGGGAGCTGTCACGGATGCAGG-3'	IDT	N/A - custom
scaffold 5'-Cy3-labeled nontemplate strand: 5'-Cy3- TATAATGGGAGCTGTCACGGATGCAGG-3'	IDT	N/A - custom
scaffold template strand for RPo, RPitc2, RPitc3, and RPitc4: 5'-CCTGCATCCGTGAGTCCAGGG-3'	IDT	N/A - custom
Recombinant DNA		
pET30a- <i>Mtb</i> -σ ^A	Jacques et al., 2006	pSR01
pET30a- <i>Mtb</i> -σ ^A (ΔR1.1)	This paper	N/A
pACYC- <i>rpoA</i>	Banerjee et al., 2014	N/A
pACYC- <i>rpoA</i> -sigA	Banerjee et al., 2014	N/A
pCOLADuet- <i>rpoB</i> - <i>rpoC</i>	Banerjee et al., 2014	N/A
pETDuet- <i>rpoB</i> - <i>rpoC</i>	Banerjee et al., 2014	N/A
pCDF- <i>rpoZ</i>	Banerjee et al., 2014	N/A
pET28a	EMD Millipore	Cat# 69864

(Continued on next page)

Continued

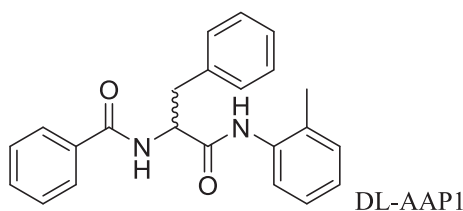
REAGENT or RESOURCE	SOURCE	IDENTIFIER
pET28a-β'MtbSI	This paper	N/A
Software and Algorithms		
Fluctuation Analysis Calculator (FALCOR)	Hall et al., 2009	http://www.keshavsingh.org/protocols/FALCOR.html
HKL2000	Otwinowski and Minor, 1997	http://www.hkl-xray.com/
Molrep	CCP4, 1994	http://www ccp4.ac.uk/html/molrep.html
Coot	Emsley et al., 2010	https://www2.mrc-lmb.cam.ac.uk/personal/pemsley/coot/
Phenix	Adams et al., 2010	https://www.phenix-online.org/
Other		
ChiralPak IA HPLC column	ChiralPak	Cat# 80325
Jupiter C18 HPLC column	Phenomenex	Cat# 00G-4055-N0
EmulsiFlex-C5 cell disrupter	Avestin	N/A
MonoQ 10/100 GL column	GE Healthcare	Cat# 17-5167-01
Amicon Ultra-15 30K centrifugal filters	EMD Millipore	Cat# UFC903024
HiLoad 16/60 Superdex 200 prep grade column	GE Healthcare	Cat# 17-1069-01
Amicon Ultra-15 10K centrifugal filters	EMD Millipore	Cat# UFC901008
Veriti PCR thermal cycler	Thermo Fisher/Applied Biosystems	Cat# 4384638
GENios Pro microplate reader	Tecan	N/A
Gryphon liquid handling system	Art Robbins	N/A

CONTACT FOR REAGENT AND RESOURCE SHARING

Requests for further information or reagents should be directed to the lead contact and corresponding author, Richard H. Ebright (ebright@waksman.rutgers.edu).

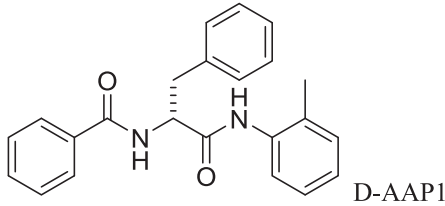
METHOD DETAILS

N_α-benzoyl-N-(2-methylphenyl)-D/L-phenylalaninamide (DL-AAP1)



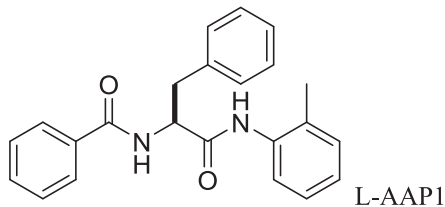
D/L-Benzoyl phenylalanine (32.2 mg; 120 μmol; Chem-Impex) was dissolved in 2 mL anhydrous dimethylformamide at 25°C. To the solution, was added PS-carbodiimide (180 mg, 240 μmol; Biotage) and hydroxybenzotriazole (24.3 mg; 180 μmol; Sigma-Aldrich). The reaction mixture was stirred for 15 min under argon, o-toluidine (10.63 μL, 100 μmol; Sigma-Aldrich) was added, and stirring was continued for 2 hr. The mixture was filtered through a plug of glass wool and evaporated to dryness. The sample was re-dissolved in chloroform and purified by silica chromatography with chloroform as eluent. Yield: 31.9 mg, 89%. ¹H-NMR (500 MHz, CDCl₃): δ 2.18 (s, 3H), 3.25 (dd, 1H), 3.35 (dd, 1H), 5.05 (dd, 1H), 6.8–7.8 (m; 14H, aryl protons). MS (MALDI): calculated: m/z 359.43 (MH⁺); found: 359.35, 381.33 (M+Na⁺).

N α -benzoyl-N-(2-methylphenyl)-D-phenylalaninamide (D-AAP1)



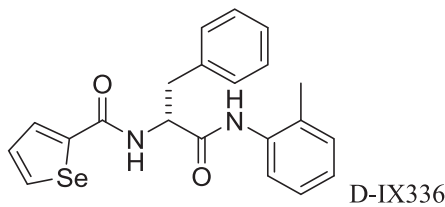
D-AAP1 was prepared as for DL-AAP1, but using D-benzoyl phenylalanine (Chem-Impex) in place of D/L-benzoyl phenylalanine. The product (100 μ g) was dissolved in isopropanol (100 μ L) and purified by chiral HPLC on a 4.6 \times 250 mm ChiralPak IA column (ChiralPak) in 10% isopropanol in hexanes at 1 mL/min. Two peaks were observed, one exhibiting a retention time of 14 min and an integrated area of 1.1 arbitrary units (assigned as the D stereoisomer, D-AAP1; 10% enantiomeric excess), and another exhibiting a retention time of 17 min and an integrated area of 1.0 arbitrary unit (assigned as the L stereoisomer, L-AAP1). The peak assigned as the D stereoisomer was collected. MS (MALDI): calculated: m/z 359.43 (MH^+); found: 359.35, 381.33 ($M+Na^+$). Optical rotation in dimethylformamide, $[\alpha]_{589}^{220C} = +19$.

N α -benzoyl-N-(2-methylphenyl)-L-phenylalaninamide (L-AAP1)



L-AAP1 was prepared as for D-AAP1, but using L-benzoyl phenylalanine (Chem-Impex) in place of D-benzoyl phenylalanine. Two peaks were observed, one exhibiting a retention time of 14 min and an integrated area of 1.0 arbitrary unit (assigned as the D stereoisomer, D-AAP1), and another exhibiting a retention time of 17 min and an integrated area of 1.1 arbitrary units (assigned as the L stereoisomer, L-AAP1; 10% enantiomeric excess). The peak assigned as the L stereoisomer was collected. MS (MALDI): calculated: m/z 359.43 (MH^+); found: 359.35, 381.33 ($M+Na^+$). Optical rotation in dimethylformamide, $[\alpha]_{589}^{220C} = -22$.

N α -selenophenoyl-N-(2-methylphenyl)-D-phenylalaninamide (D-IX336)



To a suspension of N-Fmoc-D-phenylalanine (2 g, 5.16 mmol; Chem-Impex) in 20 mL dichloromethane was added oxalyl chloride (0.66 mL, 7.74 mmol; Sigma-Aldrich) and 200 μ L dimethylformamide. After stirring for 30 min, the reaction mixture was evaporated to dryness (to remove any trace of unreacted oxalyl chloride) and re-dissolved in 30 mL dichloromethane. O-toluidine (0.554 mL, 5.16 mm; Sigma-Aldrich) was added drop-wise followed by addition of DIPEA (1.08 mL, 6.19 mm). The reaction was stirred for 2 hr, and 0.5 M HCl was used to acidify the mixture, which was then extracted with 3 \times 30 mL dichloromethane. The organic extract was filtered, washed with brine, dried with anhydrous sodium sulfate, and evaporated to a solid, providing (9H-fluoren-9-yl) methyl (R)-(1-oxo-3-phenyl-1-(o-tolylamino) propan-2-yl) carbamate, which was used without purification in the next step. Crude yield: 1.2 g, 49%. MS (MALDI): calculated: m/z 476.58 (MH^+); found: 477.13.

To 0.2 g (9H-fluoren-9-yl) methyl (R)-(1-oxo-3-phenyl-1-(o-tolylamino)-propan-2-yl) carbamate in 15 mL dichloromethane was added 0.16 mL piperidine. The reaction mixture was stirred for 6 hr, evaporated, and purified by silica chromatography with 2% methanol in dichloromethane. The lower-eluting fractions were pooled and re-purified by silica chromatography (25%–100% ethyl acetate/hexanes), providing (R)-2-amino-3-phenyl-N-(o-tolyl)propanamide. Yield: 17.6 mg, 17%. MS (MALDI): calculated: *m/z* 412.36 (MH^+); found: 413.01, 06, 434.99 ($\text{M}+\text{Na}^+$).

To (R)-2-amino-3-phenyl-N-(o-tolyl)-propanamide (17.6 mg, 69 μmol) in 0.5 mL dichloromethane, was added selenophene-2-carboxylic acid (18.2 mg in 0.5 mL dichloromethane, 104 μmol ; LabNetwork), DIPEA (18.2 μl , 104 μmol) and propane phosphonic acid anhydride (T3P; 88.6 μl , 140 μmol ; Sigma-Aldrich as 50% solution in ethyl acetate). The reaction mixture was stirred for 22 hr and then evaporated to an oil. The resulting oil was re-dissolved in 10 mL ethyl acetate, washed with 5 mL 0.5 M HCl, 5 mL saturated sodium bicarbonate, 5 mL brine, dried with anhydrous sodium sulfate, and evaporated to dryness. The crude material was purified by semi-preparative reverse-phase HPLC (25 \times 10 mm Jupiter C18, 10 μm , 300 \AA ; 30%–60% B in 30 min; A = 0.1% trifluoroacetic acid; B = 0.1% trifluoroacetic acid in acetonitrile; 4 ml/min; Phenomenex), providing D-IX336. Yield: 7 mg, 25%. MS (MALDI): calculated: *m/z* 254.33 (MH^+); found: 255.06, 277.03 ($\text{M}+\text{Na}^+$). $^1\text{H-NMR}$ (500 MHz, CDCl_3): δ 8.22 (d, 1H), 7.79 (d, 1H), 7.65 (s, 1H), 7.55 (br s, 1H), 7.00–7.40 (m, 9H), 6.70 (d, 1H), 4.80 (m, 1H), 3.20 (dd, 1H), 3.38 (dd, 1H), 1.99 (s, 3H).

***M. tuberculosis* σ^Δ**

E. coli strain BL21(DE3) (Invitrogen) was transformed with plasmid pET30a-*Mtb*- σ^Δ (Jacques et al., 2006), encoding N-terminally hexahistidine-tagged *Mtb* σ^Δ under control of the bacteriophage T7 gene 10 promoter. Single colonies of the resulting transformants were used to inoculate 50 mL LB broth containing 50 $\mu\text{g}/\text{ml}$ kanamycin, and cultures were incubated 16 hr at 37°C with shaking. Aliquots (10 ml) were used to inoculate 1 L LB broth containing 50 $\mu\text{g}/\text{ml}$ kanamycin, cultures were incubated at 37°C with shaking until $\text{OD}_{600} = 0.8$, cultures were induced by addition of IPTG to 1 mM, and cultures were incubated overnight at 16°C. Cells were harvested by centrifugation (4,000 $\times g$; 15 min at 4°C), re-suspended in 20 mL buffer A (10 mM Tris-HCl, pH 7.9, 0.2 M NaCl, 5% glycerol), and lysed using an EmulsiFlex-C5 cell disrupter (Avestin). The lysate was centrifuged (20,000 $\times g$; 30 min at 4°C), and the supernatant was loaded onto a 5 mL column of Ni-NTA-agarose (QIAGEN, Inc.) equilibrated in buffer A. The column was washed with 50 mL buffer A containing 40 mM imidazole and eluted with 25 mL buffer A containing 250 mM imidazole. The sample was further purified by anion-exchange chromatography on a Mono Q column 10/100 GL (GE Healthcare; 160 mL linear gradient of 300–500 mM NaCl in 10 mM Tris-HCl, pH 7.9, 0.1 mM EDTA, 5 mM dithiothreitol, and 5% glycerol; flow rate = 1 ml/min). Fractions containing σ^Δ were pooled, were concentrated to ~15 mg/ml using 30 kDa MWCO Amicon Ultra-15 centrifugal ultrafilters (Millipore) and stored at –80°C. Yields were ~10 mg/L, and purities were >95%.

Mtb σ^Δ (ΔR1.1) was prepared analogously, using plasmid pET30a-*Mtb*- σ^Δ (ΔR1.1), encoding N-terminally hexahistidine-tagged *Mtb* σ^Δ (225–528) under control of the bacteriophage T7 gene 10 promoter [constructed by replacing the EcoRI-NotI segment of plasmid pET30a (EMD Millipore) by the EcoRI-NotI DNA segment of a DNA fragment carrying TTAGAATTC, followed by codons 225–528 of *Mtb sigA*, followed by TAAGCGGCCGCTAA, generated by PCR with plasmid pET30a-*Mtb*- σ^Δ as template].

***M. tuberculosis* β' MtbSI**

E. coli strain BL21(DE3) (Invitrogen) was transformed with plasmid pET28a- β' MtbSI, encoding N-hexahistidine-tagged β' MtbSI under control of the bacteriophage T7 gene 10 promoter [constructed by replacing the *Nde*I-EcoRI segment of plasmid pET28a (EMD Millipore) with the *Nde*I-EcoRI DNA segment of a DNA fragment carrying TTACATATG, followed by codons 141–229 of *Mtb rpoC*, followed by TAAGAATTCTAA, generated by PCR with plasmid pCOLADuet-*rpoB-rpoC* (Banerjee et al., 2014) as template]. Single colonies of the resulting transformants were used to inoculate 50 mL LB broth containing 50 $\mu\text{g}/\text{ml}$ kanamycin, and cultures were incubated 16 hr at 37°C with shaking. Aliquots (10 ml) were used to inoculate 1 L LB broth containing 50 $\mu\text{g}/\text{ml}$ kanamycin, cultures were incubated at 37°C with shaking until $\text{OD}_{600} = 0.8$, cultures were induced by addition of IPTG to 1 mM, and cultures were incubated overnight at 16°C. Cells were harvested by centrifugation (4,000 $\times g$; 15 min at 4°C), re-suspended in 20 mL buffer A (10 mM Tris-HCl, pH 7.9, 0.2 M NaCl, 5% glycerol), and lysed using an EmulsiFlex-C5 cell disrupter (Avestin). The lysate was centrifuged (20,000 $\times g$; 30 min at 4°C), and the supernatant was loaded onto a 5 mL column of Ni-NTA-agarose (QIAGEN) equilibrated in buffer A. The column was washed with 50 mL buffer A containing 40 mM imidazole and eluted with 25 mL buffer A containing 250 mM imidazole. The sample was further purified using by gel filtration on a HiLoad 16/60 Superdex 200 prep grade column (GE Healthcare, Inc) in 20 mM Tris-HCl, pH 8.0, 75 mM NaCl, 5 mM MgCl₂, and was concentrated to ~10 mg/L in the same buffer using 10 kDa MWCO Amicon Ultra-15 centrifugal ultrafilters (Millipore) and stored at –80°C. Yields were ~20 mg/L, and purities were >95%.

Selenomethionine-substituted β' MtbSI protein was produced using plasmid pET28a- β' MtbSI and the procedures of Stols et al., 2004 and was purified as for native β' MtbSI.

***M. tuberculosis* RNAP Core Enzyme**

Mtb RNAP core enzyme and RNAP core enzyme derivatives were prepared from cultures of *E. coli* strain BL21(DE3) (Invitrogen) co-transformed with plasmids pACYC-*rpoA*, pCOLADuet-*rpoB-rpoC*, and pCDF-*rpoZ* (Banerjee et al., 2014), or derivatives thereof constructed using site-directed mutagenesis (QuikChange Kit; Agilent Technologies), using procedures as in Banerjee et al., 2014.

***M. tuberculosis* σ^A Holoenzyme**

Mtb RNAP σ^A holoenzyme and RNAP σ^A holoenzyme derivatives were prepared from cultures of *E. coli* strain BL21(DE3) (Invitrogen) co-transformed with plasmids pACYC-*rpoA-sigA*, pETDuet-*rpoB-rpoC* and pCDF-*rpoZ* (Banerjee et al., 2014), or derivatives thereof constructed using site-directed mutagenesis (QuikChange Kit; Agilent Technologies), using procedures as in Banerjee et al., 2014.

Oligonucleotides

Oligodeoxyribonucleotides (Integrated DNA Technologies) and oligoribonucleotides (GpA, GpGpA, and UpCpGpA; Trilink) were dissolved in nuclease-free water (Ambion) to 3 mM and stored at -80°C .

Nucleic-Acid Scaffolds

Nucleic-acid scaffolds RPo, RPitc3, and RPitc4 (sequences in Figure 1A) were prepared as follows: Nontemplate-strand oligodeoxyribonucleotide (0.5 mM), template-strand oligodeoxyribonucleotide (0.55 mM), and, where indicated, 3 nt or 4 nt oligoribonucleotide (1 mM) in 40 μl 5 mM Tris-HCl, pH 7.7, 0.2 M NaCl, and 10 mM MgCl₂ were heated 5 min at 95°C , cooled to 25°C in 2°C steps with 1 min per step using a thermal cycler (Applied Biosystems), and stored at -80°C .

RNAP-DNA Interaction Assays

Stabilities of *Mtb* RPo were assessed using fluorescence polarization assays (Heyduk et al., 1996) in a 96-well microplate format. Reaction mixtures contained (100 μl): 0–320 μM *Mtb* RNAP σ^A holoenzyme or derivative, 10 nM Cy3-labeled nucleic-acid scaffold RPo (sequence in Figure 1A; Cy3 incorporated at 5' end of nontemplate strand), 20 mM Tris-HCl, pH 8.0, 250 mM NaCl, 5 mM MgCl₂, and 5 mM dithiothreitol. Reaction mixtures were incubated 10 min at 25°C , and fluorescence emission intensities were measured using a microplate reader equipped with polarizers (GENios Pro; Tecan Trading; excitation wavelength = 550 nm; emission wavelength = 570 nm). Fluorescence polarization was calculated using:

$$P = (I_{VW} - I_{VH}) / (I_{VW} + I_{VH}) \quad (1)$$

where I_{VW} and I_{VH} are fluorescence intensities with the excitation polarizer at the vertical position and the emission polarizer at, respectively, the vertical position and the horizontal position.

Equilibrium dissociation constants, K_D , were extracted by non-linear regression using:

$$P = P_o + \{(P_b - P_o) \times [R] / (K_D + [R])\} \quad (2)$$

where P is fluorescence polarization at RNAP concentration R, P_o is fluorescence polarization in the absence of RNAP, and P_b is the fluorescence polarization in the presence of a saturating RNAP concentration.

RNAP-Inhibitory Activities

Fluorescence-detected RNAP-inhibition assays were performed using the profluorescent substrate γ -[2'-(2-benzothiazoyl)-60-hydroxybenzothiazole]-ATP [BBT-ATP; Jena Bioscience; procedures as in Feng et al., 2015], using 150 nM *Mtb* RNAP core enzyme plus 600 nM *Mtb* σ^A , 75 nM *Eco* RNAP σ^{70} holoenzyme (prepared as in Zhang et al., 2014), or 75 nM *S. aureus* RNAP core enzyme and 300 nM *S. aureus* σ^A (prepared as in Srivastava et al., 2011) and 20 nM DNA fragment containing bacteriophage T5 N25 promoter (prepared as in Zhang et al., 2014).

Radiochemical assays with human RNAP I/II/III were performed as in Degen et al., 2014.

Half-maximal inhibitory concentrations (IC_{50} s) were calculated by non-linear regression in SigmaPlot (SPSS, Chicago, IL).

Growth-Inhibitory Activities

Minimal inhibitory concentrations (MICs) for *Mtb* H37Rv and *M. avium* ATCC 25291 were quantified in microplate Alamar Blue assays (procedures as in Collins and Franzblau, 1997).

MICs for *M. smegmatis* mc²155, *M. smegmatis* ATCC 19420, and derivatives thereof were quantified in broth microdilution assays [procedures essentially as in CLSI/NCCLS (2009)], using 7H9 broth (BD Biosciences) supplemented with 0.5% glycerol, and 0.05% Tween80, and using a starting cell density of 2.5×10^5 cfu/ml, and incubation 72 hr at 37°C .

MICs for *Staphylococcus aureus* ATCC 12600, *Escherichia coli* D21f2toIC, and mammalian cells (Vero E6) were determined as in Degen et al., 2014.

Resistance and Cross-Resistance Assays

M. smegmatis mc²155 (*rpoB*'637'A), a derivative of *M. smegmatis* mc²155 having a chromosomal *rpoB* gene that encodes a derivative of RNAP β subunit having a substitution corresponding to Eco β R637A, was constructed using recombineering with targeting oligonucleotide 5'-GGCGGAGACGAAGCTCGACCTCGCCGCCCTCTGGCGACCATGACGGGTCTCGGTGAAGCGGCC GTTCTC-3' [procedures as in Murphy et al., 2015; selected on Seven H11 agar (BD Biosciences) containing Middlebrook ADC enrichment (BD Biosciences), 0.5% glycerol, and 30 $\mu\text{g}/\text{ml}$ D-AAP1; confirmed by PCR amplification and sequencing of *rpoB* and *rpoC*].

M. smegmatis ATCC 19420 (*rpoB*'526'Y) and ATCC 19420 (*rpoB*'531'L), ATCC 19420 derivatives having chromosomal *rpoB* genes that encode RNAP β subunits having substitutions that correspond to *Eco* β H526Y and *Eco* β S531L, were obtained as spontaneous Rif-resistant mutants (selected on Seven H11 agar containing Middlebrook ADC enrichment, 0.5% glycerol, and 50 µg/ml Rif; confirmed by PCR amplification and sequencing of *rpoB* and *rpoC*].

Resistance and cross-resistance levels were determined in broth microdilution assays (see above, “Growth-inhibitory activities”), using final concentrations of 0.0015–50 µg/ml D-AAP1 or Rif.

Checkerboard Interaction Assays

To assess antibacterial activities of combinations of D-AAP1 and Rif, broth-microdilution assays with *M. smegmatis* ATCC 19420 (see above, “Growth inhibitory activities”) were performed in a checkerboard format (Horrevorts et al., 1987; White et al., 1996; Meletiadis et al., 2010), analyzing in quintuplicate, all pairwise combinations of D-AAP1 at 4.00x, 3.50x, 3.00x, 2.67x, 2.63x, 2.50x, 2.33x, 2.25x, 2.00x, 1.88x, 1.75x, 1.67x, 1.50x, 1.33x, 1.25x, 1.13x, 1.00x, 0.750x, 0.667x, 0.500x, 0.375x, 0.333x, and 0.250 MIC ($\text{MIC}_{\text{D-AAP1}} = 0.20 \mu\text{g/ml}$) with Rif at 1.33x, 1.17x, 1.00x, 0.875x, 0.833x, 0.750x, 0.667x, 0.656x, 0.625x, 0.500x, 0.469x, 0.375x, 0.333x, 0.281x, 0.250x, 0.188x, 0.167x, 0.125x, and 0.094x MIC ($\text{MIC}_{\text{Rif}} = 3.13 \mu\text{g/ml}$). Minimum and maximum fractional inhibitory concentrations indices (FICI_{max} and FICI_{min}) were calculated as in White et al. (1996). $\text{FICI}_{\text{min}} \leq 0.5$ was deemed indicative of super-additivity (synergism), $\text{FICI}_{\text{min}} > 0.5$ and $\text{FICI}_{\text{max}} \leq 4.0$ was deemed indicative of additivity, and $\text{FICI}_{\text{max}} > 4.0$ was deemed indicative of sub-additivity (antagonism) (White et al., 1996; Meletiadis et al., 2010).

Resistance-Rate Assays

Resistance rates were determined using fluctuation assays essentially as in Srivastava et al., 2012. Defined numbers of cells of *M. smegmatis* ATCC 19420 (~10⁹ cfu/plate) were plated on Seven H11 agar containing Middlebrook ADC enrichment, 0.5% glycerol, and either 1.56 µg/ml D-AAP1, 50 µg/ml Rif, or both 1.56 µg/ml D-AAP1 and 50 µg/ml Rif; and numbers of colonies were counted after 72 hr at 37°C (at least 4 determinations for each concentration of each test compound). Resistance rates were calculated using the Ma-Sandri-Sarkar Maximum Likelihood Estimator (Ma et al., 1992; Sarkar et al., 1992) as implemented on the Fluctuation Analysis Calculator (FALCOR; <http://www.keshavsingh.org/protocols/FALCOR.html>; Hall et al., 2009). Sampling correction was performed as in Stewart et al. (1990).

Structure Determination: Assembly of Transcription Initiation Complexes

For *Mtb* RPo, RPItc3, and RPItc4, complexes for crystallization were prepared by mixing 16 µl 50 µM *Mtb* RNAP σ^A holoenzyme (in 20 mM Tris-HCl, pH 8.0, 75 mM NaCl, 5 mM MgCl₂, and 5 mM dithiothreitol) and 4 µl 0.4 mM of nucleic-acid scaffold RPo, RPItc3, or RPItc4 (in 5 mM Tris-HCl, pH 7.7, 0.2 M NaCl, and 10 mM MgCl₂) and incubating 1 hr at 25°C. For *Mtb* RPItc2, the complex for crystallization was prepared by mixing 16 µl 50 µM *Mtb* RNAP holoenzyme (in 20 mM Tris-HCl, pH 8.0, 75 mM NaCl, 5 mM dithiothreitol, 5 mM MgCl₂), 4 µl 0.4 mM of nucleic-acid scaffold RPo (in 5 mM Tris-HCl, pH 7.7, 0.2 M NaCl, and 10 mM MgCl₂), and 1 µl 25 mM GpA (in water), and incubating 1 hr at 25°C. For *Mtb* RPo, RPItc3, and RPItc4 in complex with Rif, complexes for crystallization were prepared by incubating 16 µl 50 µM *Mtb* RNAP σ^A holoenzyme (in 20 mM Tris-HCl, pH 8.0, 75 mM NaCl, 5 mM MgCl₂, and 5 mM dithiothreitol,) and 0.5 µl 8 mM Rif (Sigma-Aldrich), 0.5 hr at 25°C, and then adding 4 µl 0.4 mM of nucleic-acid scaffold RPo, RPItc3, or RPItc4 (in 5 mM Tris-HCl, pH 7.7, 0.2 M NaCl, and 10 mM MgCl₂), and incubating 1 hr at 25°C. For *Mtb* RPItc2 in complex with Rif, the complex for crystallization was prepared by incubating 16 µl 50 µM *Mtb* RNAP σ^A holoenzyme (in 20 mM Tris-HCl, pH 8.0, 75 mM NaCl, 5 mM MgCl₂, and 5 mM dithiothreitol) and 0.5 µl 8 mM Rif, 0.5 hr at 25°C, and then adding 4 µl 0.4 mM of nucleic-acid scaffold RPo (in 5 mM Tris-HCl, pH 7.7, 0.2 M NaCl, and 10 mM MgCl₂) and 1 µl 25 mM GpA (in water) and incubating 1 hr at 25°C.

Structure Determination: Crystallization, Cryo-cooling, and Crystal Soaking

Robotic crystallization trials were performed for *Mtb* RPo and β'MtbSI using a Gryphon liquid handling system (Art Robbins Instruments), commercial screening solutions (Emerald/Rigaku, Hampton Research, and QIAGEN), and the sitting-drop vapor diffusion technique [drop: 0.2 µl transcription initiation complex (previous section) or 0.2 µl 500 µM β'MtbSI (in 20 mM Tris-HCl, pH 8.0, 75 mM NaCl, 5 mM MgCl₂, and 5 mM dithiothreitol) plus 0.2 µl screening solution; reservoir: 60 µl screening solution; 22°C]. 900 conditions were screened. Under several conditions, *Mtb* RPo crystals appeared within two weeks, and β'MtbSI crystals appeared within one week. Conditions were optimized using the hanging-drop vapor-diffusion technique at 22°C. The optimized conditions for *Mtb* RPo (drop: 1 µl RPo in 20 mM Tris-HCl, pH 8.0, 75 mM NaCl, 5 mM MgCl₂, and 5 mM dithiothreitol plus 1 µl 50 mM Tris-HCl, pH 8.2, 200 mM KCl, 50 mM MgCl₂, and 10% PEG3350 plus 0.2 µl 80.0 mM CHAPSO; reservoir: 400 µl 50 mM Tris-HCl, pH 8.2, 200 mM KCl, 50 mM MgCl₂, and 10% PEG3350; 22°C) yielded high-quality, rod-like crystals with dimensions of 0.4 mm x 0.1 mm x 0.1 mm in two weeks (Figure 1A). The optimized conditions for β'MtbSI were as follows: drop: 1 µl β'MtbSI in 20 mM Tris-HCl, pH 8.0, 75 mM NaCl, 5 mM MgCl₂ and 5 mM dithiothreitol plus 1 µl 100 mM sodium citrate tribasic dihydrate, pH 5.5, and 22% PEG1000; reservoir: 400 µl 100 mM sodium citrate tribasic dihydrate, pH 5.5, and 22% PEG1000; 22°C. *Mtb* RPo and β'MtbSI crystals were transferred to reservoir solution containing 18% (v/v) (2R,3R)-(-)-2,3-butanediol (Sigma-Aldrich) and flash-cooled with liquid nitrogen. Analogous procedures were used for *Mtb* RPItc2, RPItc3, RPItc4, and complexes with Rif.

For *Mtb* RPo in complex with D-AAP1 or D-IX336, *Mtb* RPo crystals were soaked by adding 0.2 μ l 20 mM D-AAP1 or D-IX336 in (2R,3R)-(-)-2,3-butanediol directly into the drop for 2 hr, transferring to reservoir solution containing 18% (v/v) (2R,3R)-(-)-2,3-butanediol, and flash-cooling with liquid nitrogen. For *Mtb* RPo in complex with both Rif and D-AAP1, pre-formed crystals of *Mtb* RPo-Rif were soaked by adding 0.2 μ l 20 mM of D-AAP1 in (2R,3R)-(-)-2,3-butanediol directly into the drop for 2 hr, transferring to reservoir solution containing 18% (v/v) (2R,3R)-(-)-2,3-butanediol, and flash-cooling with liquid nitrogen.

Structure Determination: Data Collection and Reduction

Diffraction data and selenium single-wavelength anomalous dispersion data were collected from cryo-cooled crystals at Argonne National Laboratory beamline 19ID-D. Data were processed using HKL2000 ([Otwinowski and Minor, 1997](#)). The resolution cut-off criteria were $I/\sigma > 1.3$ and $R_{\text{merge}} < 1$.

Structure Determination: Structure Solution and Refinement

The structure of *Mtb* RPo was solved by molecular replacement with Molrep ([CCP4, 1994](#)) using the structure of *T. thermophilus* RPo (PDB: 4G7H; [Zhang et al., 2012](#)) as the search model. One RNAP molecule was present in the asymmetric unit. Early-stage refinement included rigid-body refinement of RNAP, followed by rigid-body refinement of RNAP subunits, followed by rigid-body refinement of 44 RNAP domains (methods as in [Zhang et al., 2012](#)). Electron density for nucleic acids was unambiguous, but was not included in models in early-stage refinement. Cycles of iterative model building with Coot ([Emsley et al., 2010](#)) and refinement with Phenix ([Adams et al., 2010](#)) were performed. Improvement of the coordinate model resulted in improvement of phasing, and electron density maps for nucleic acids, which were not included in models at this stage of model building and refinement, improved over successive cycles. Nucleic acids then were built into the model and refined in stepwise fashion. The final model was generated by XYZ-coordinate refinement with secondary-structure restraints, followed by group B-factor and individual B-factor refinement. The final model, refined to R_{work} and R_{free} of 0.22 and 0.27, respectively, was deposited in the PDB with accession code PDB: 5UHA ([Table 1](#)). Analogous procedures were used to solve and refine structures of *Mtb* RPItc2, RPItc3, and RPItc4 ([Table 1](#)). Analogous procedures were used to solve and preliminarily refine structures of complexes with inhibitors; models of inhibitors then were built into mF_o-DF_c difference maps, and additional cycles of refinement and model building were performed, ([Table 1](#)).

The structure of $\beta'MtbSI$ was solved by the single-wavelength anomalous dispersion method, using Autosol as implemented in Phenix ([Adams et al., 2010](#)). The structure model was built using the program Coot ([Emsley et al., 2010](#)), and structure refinement was carried out using Phenix ([Adams et al., 2010](#)). The final model was refined to 2.2 Å resolution ([Table 1](#)).

QUANTITATION AND STATISTICAL ANALYSIS

Data for RNAP-DNA-interaction assays are means and SEMs for at least three replicates. Data for RNAP-inhibitory activities, growth-inhibitory activities, resistance, and cross-resistance are means of at least two determinations. Data for checkerboard interaction assays and resistance-rate assays are means and 95% confidence intervals for at least five and at least four replicates, respectively. The accession numbers for the structures reported in this paper are PDB: 5UHA, 5UH9, 5UH5, 5UH8, 5UH6, 5UHC, 5UHD, 5UHE, 5UHF, 5UHG, and 5UH7.

Supplemental Information

Structural Basis of *Mycobacterium tuberculosis*

Transcription and Transcription Inhibition

Wei Lin, Soma Mandal, David Degen, Yu Liu, Yon W. Ebright, Shengjian Li, Yu Feng, Yu Zhang, Sukhendu Mandal, Yi Jiang, Shuang Liu, Matthew Gigliotti, Meliza Talaue, Nancy Connell, Kalyan Das, Eddy Arnold, and Richard H. Ebright

SUPPLEMENTARY FIGURES

Fig. S1 (related to Fig. 2). Recognition by *Mtb* σ^A of promoter -10 element and promoter discriminator element: interactions with nontemplate-strand positions -11 through -7.

(A) Recognition by *Mtb* σ^A of promoter -10 element: interactions with nontemplate-strand positions -11 through -7. Top, interactions with nontemplate-strand position -11. Middle, interactions with nontemplate-strand positions -10, -9, and -8. Bottom, interactions with nontemplate-strand positions -7. In left subpanels, DNA nucleotides are shown in stick representation to highlight individual protein-nucleotide interactions. In right subpanels, DNA nucleotide base moieties are shown in space-filling representations to highlight protein-base steric complementarity. Yellow surfaces, solvent-accessible surfaces of *Mtb* σ^A ; dark blue surfaces, van der Waals surfaces of DNA bases of -10 element; yellow ribbons, *Mtb* σ^A backbone; yellow, yellow-blue, and yellow-red stick representations, σ^A carbon, nitrogen, and oxygen atoms; white, blue, red, and orange stick representations, DNA carbon, nitrogen, oxygen, and phosphorous atoms; blue dashed lines, H-bonds.

(B) Recognition by *Mtb* σ^A of promoter discriminator element: interactions with nontemplate-strand positions -6 through -4. Top, interactions with nontemplate-strand position -6. Bottom, interactions with nontemplate-strand positions -5 and -4. Light blue surfaces, van der Waals surfaces of DNA bases of discriminator element. Other colors as in A.

Fig. S2 (related to Fig. 2). Recognition by *Mtb* RNAP core enzyme of promoter core recognition element (CRE): interactions with nontemplate-strand positions -4 through +2.

Gray surfaces, solvent-accessible surfaces of RNAP β subunit; light blue and pink surfaces, van der Waals surfaces of DNA bases; gray ribbons, RNAP β -subunit backbone; gray, gray-blue, and gray-red stick representations, RNAP β -subunit carbon, nitrogen, and oxygen atoms. Top, interactions with nontemplate-strand positions -4, -3 and -2. Middle, interactions with nontemplate-strand position +1. Bottom, interactions with nontemplate-strand position +2. Other colors as in Fig. S1A.

Fig. S3 (related to Fig. 3). Difference in position of σ R1.1 in RNAP holoenzyme vs. in RPo.

(A) Top subpanels, structures of *Eco* RNAP holoenzyme (left) and *Mtb* RPo (right), showing position of σ R1.1 helix 4 (H4; green in *Eco* RNAP holoenzyme and orange in *Mtb* RPo). Bottom subpanels, same as top subpanels, but showing full structure and approximate molecular volume of σ R1.1 of *Eco* RNAP holoenzyme (green ribbons and green dashed circle) and showing H4 and approximate molecular volume of σ R1.1 of *Mtb* RPo (orange ribbon and orange dashed circle). The position of σ R1.1 H4 in RPo differs from the position in RNAP holoenzyme by a \sim 100° rotation (black arrow) about a "pivot" comprising the short unstructured segment between σ R1.1 H4 and the rest of σ (black circle).

(B) Same as (A), but orthogonal view.

Fig. S4 (related to Fig 5). Preparation of D-AAP1 and D-IX336

(A) Preparation and stereospecificity of D-AAP1. Top subpanel, synthesis, chiral chromatography, and spectropolarimetry of D-AAP1 and L-AAP1 starting from D-stereoisomer precursor benzoyl-D-phenylalanine (upper half of subpanel) or starting from L-stereoisomer precursor benzoyl-L-phenylalanine (lower half of subpanel). Bottom subpanel, RNAP-inhibitory activities and antibacterial activities of DL-AAP1, D-AAP1, and L-AAP1.

(B) Preparation of selenium-containing D-AAP1 analog D-IX336.

Fig. S5 (related to Fig. 5). Relationship between binding sites of mycobacterial-specific inhibitor D-AAP1 and Gram-negative-specific inhibitor CBR703: structures.

(A) Structure of *Mtb* RPo in complex with D-AAP1. Left subpanel, overall structure. Middle subpanel, RNAP-inhibitor interactions. Right subpanel, schematic summary of RNAP-inhibitor interactions. Colors and labels as in Fig.3B.

(B) Structure of *Eco* RNAP holoenzyme in complex with CBR703 (Feng et al., 2015). Subpanels, colors and labels as in (A).

Fig. S6 (related to Fig. 5). Relationship between binding sites of mycobacterial-specific inhibitor D-AAP1 and Gram-negative-specific inhibitor CBR703: sequence alignments.

Locations of residues that contact D-AAP1 and CBR703 in the sequences of RNAP β subunit (A) and RNAP β' subunit (B). Sequence alignments for the β and β' subunits of bacterial RNAP (top 23 sequences in each panel) and corresponding subunits of human RNAP I, RNAP II, and RNAP III (bottom three sequences in each panel), showing locations of RNAP residues that contact inhibitor in both *Mtb* RPo-D-AAP1 and *Eco* RNAP-CBR703 (black rectangles; identities from Fig. S5), RNAP residue that contacts inhibitor in *Mtb* RPo-D-AAP1 but not *Eco* RNAP-CBR703 (gray rectangles; identities from Fig. S5), locations of RNAP structural elements (top row of black bars; boundaries from Lane and Darst, 2010; Weinzierl, 2010; Hein and Landick, 2010), and RNAP conserved regions (next two rows of black bars; boundaries from Lane and Darst, 2010; Sweetser et al., 1987; Jokerst et al., 1989). Species are as follows: *Mycobacterium tuberculosis* (MYCTU), *Mycobacterium avium* (MYCA1), *Mycobacterium abscessus* (MYCA9), *Mycobacterium smegmatis* (MYCSM), *Escherichia coli* (ECOLI), *Salmonella typhimurium* (SALTY), *Klebsiella pneumoniae* (KLEP7), *Enterococcus cloacae* (ENTCC), *Vibrio cholerae* (VIBCH), *Haemophilus influenzae* (HAEIN), *Neisseria gonorrhoeae* (NEIG1), *Stenotrophomonas maltophilia* (STPMP), *Moraxella catarrhalis* (MORCA), *Acinetobacter baumannii* (ACIBC), *Pseudomonas aeruginosa* (PSEAE), *Staphylococcus aureus* (STAAU), *Staphylococcus epidermidis* (STAEQ), *Enterococcus faecalis* (ENTFA), *Streptococcus pyogenes* (STRP1), *Streptococcus pneumoniae* (STRP2), *Clostridium difficile* (CDIFF), *Thermus thermophilus* (THETH), *Thermus aquaticus* (THEAQ), *Deinococcus radiodurans* (DEIRA), and *Homo sapiens* (HUMAN).

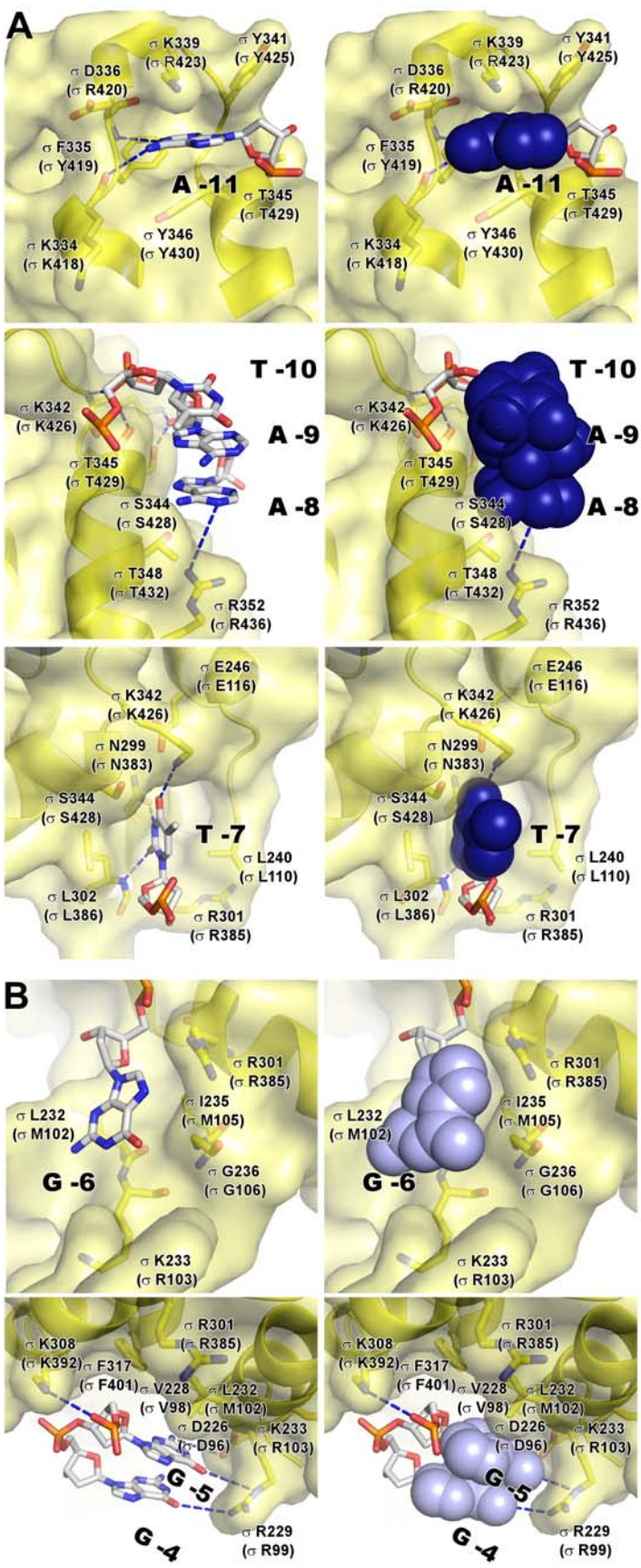


Figure S1

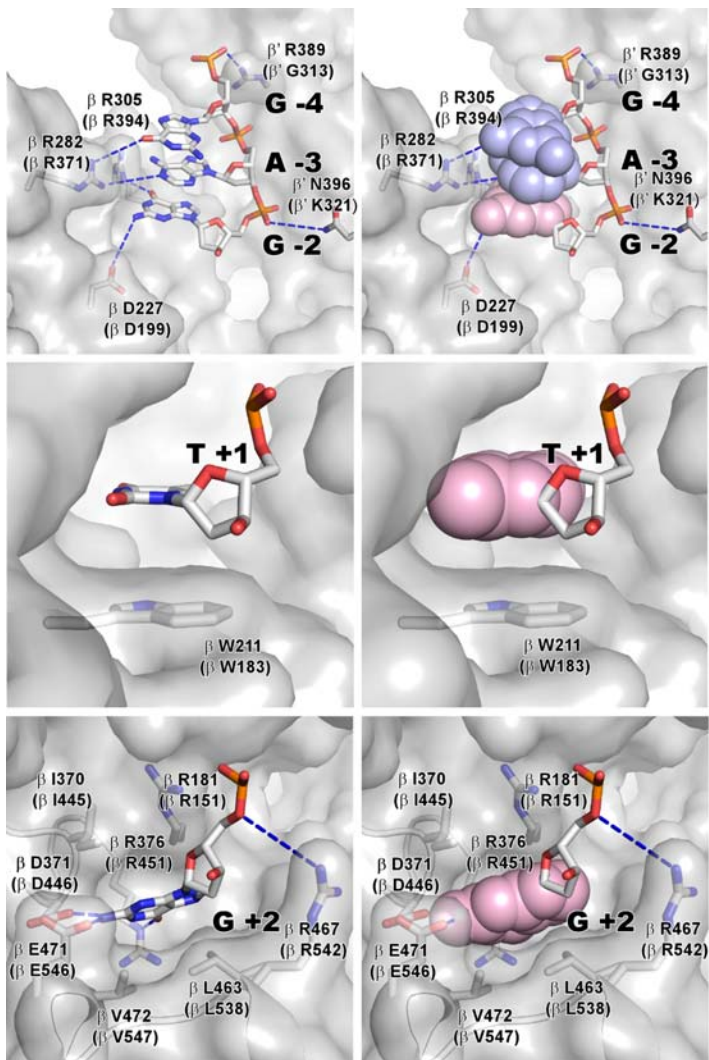
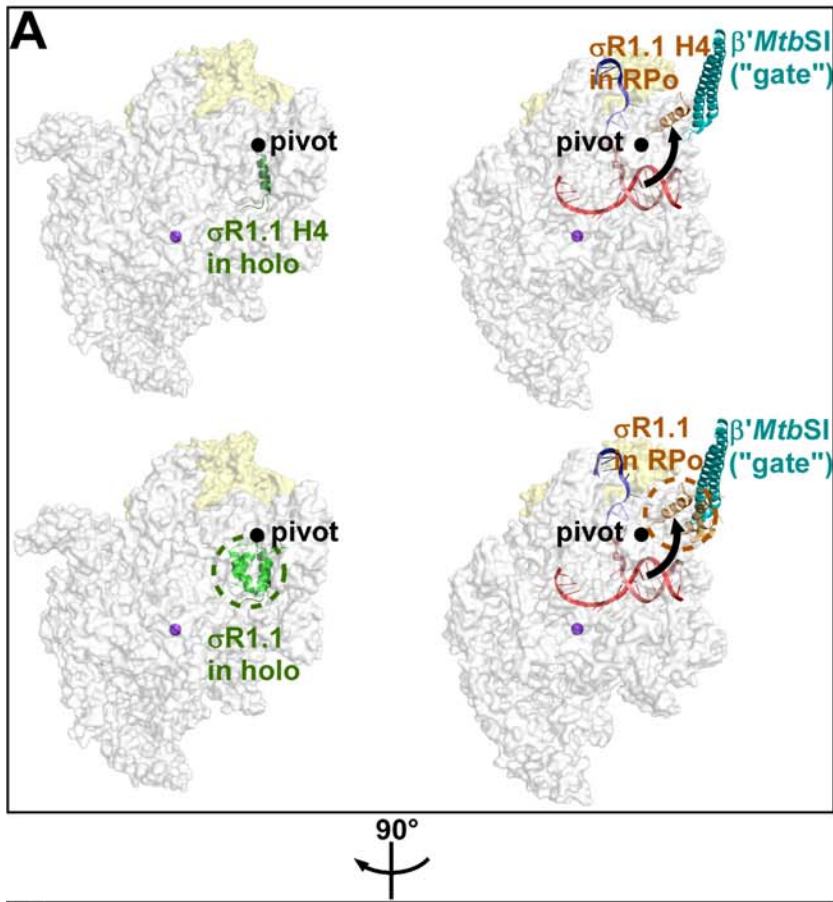


Figure S2



90°

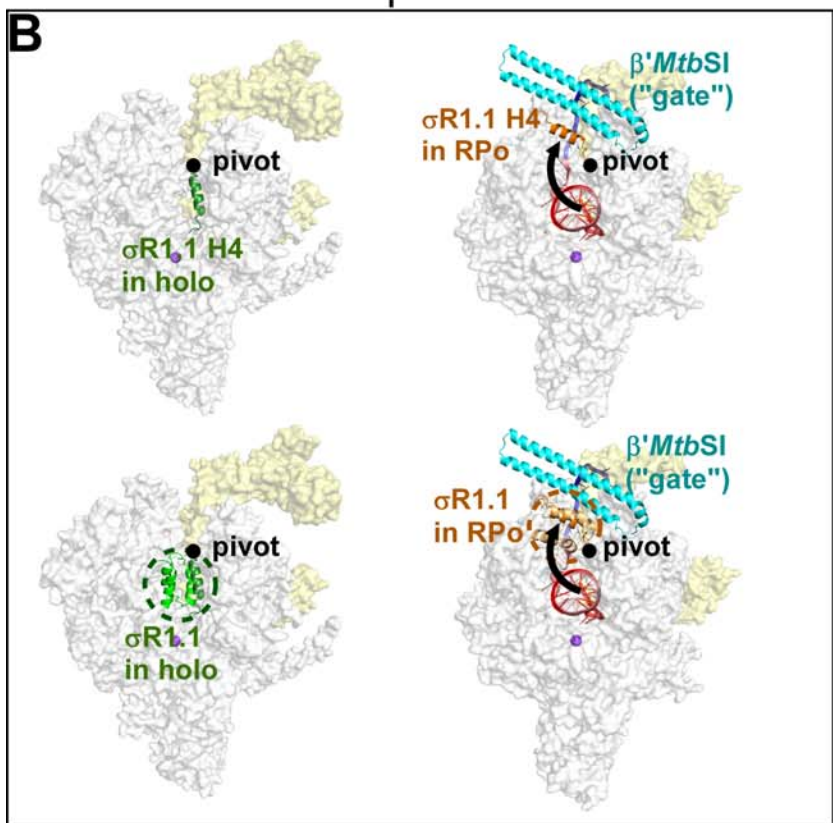
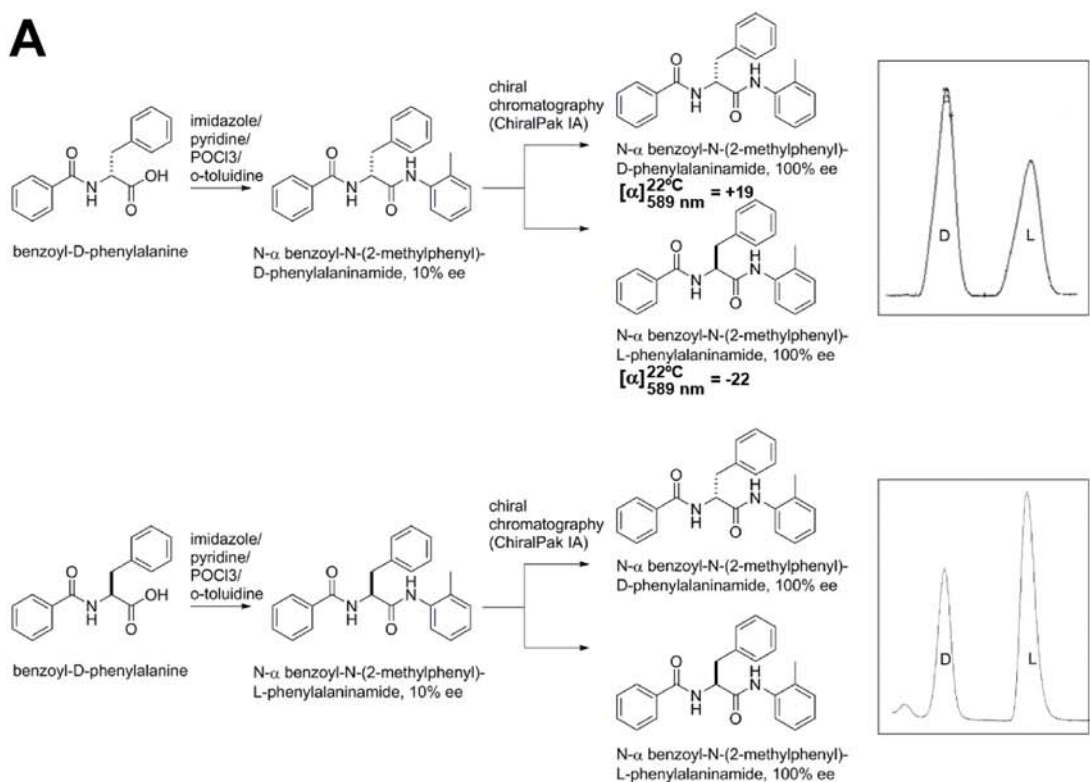


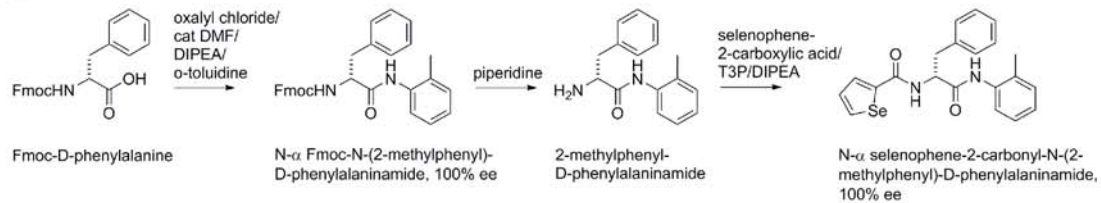
Figure S3

A
**comparison of AAP1 stereoisomers:
RNAP-inhibitory activity**

compound	Mtb RNAP IC50 (μ M)
DL-AAP1 (racemic mixture)	0.8
D-AAP1	0.4
L-AAP1	>50

**comparison of AAP1 stereoisomers:
antimycobacterial activity**

compound	Mtb H37Rv MIC (μ g/ml)
DL-AAP1 (racemic mixture)	6.25
D-AAP1	3.13
L-AAP1	>50

B**Figure S4**

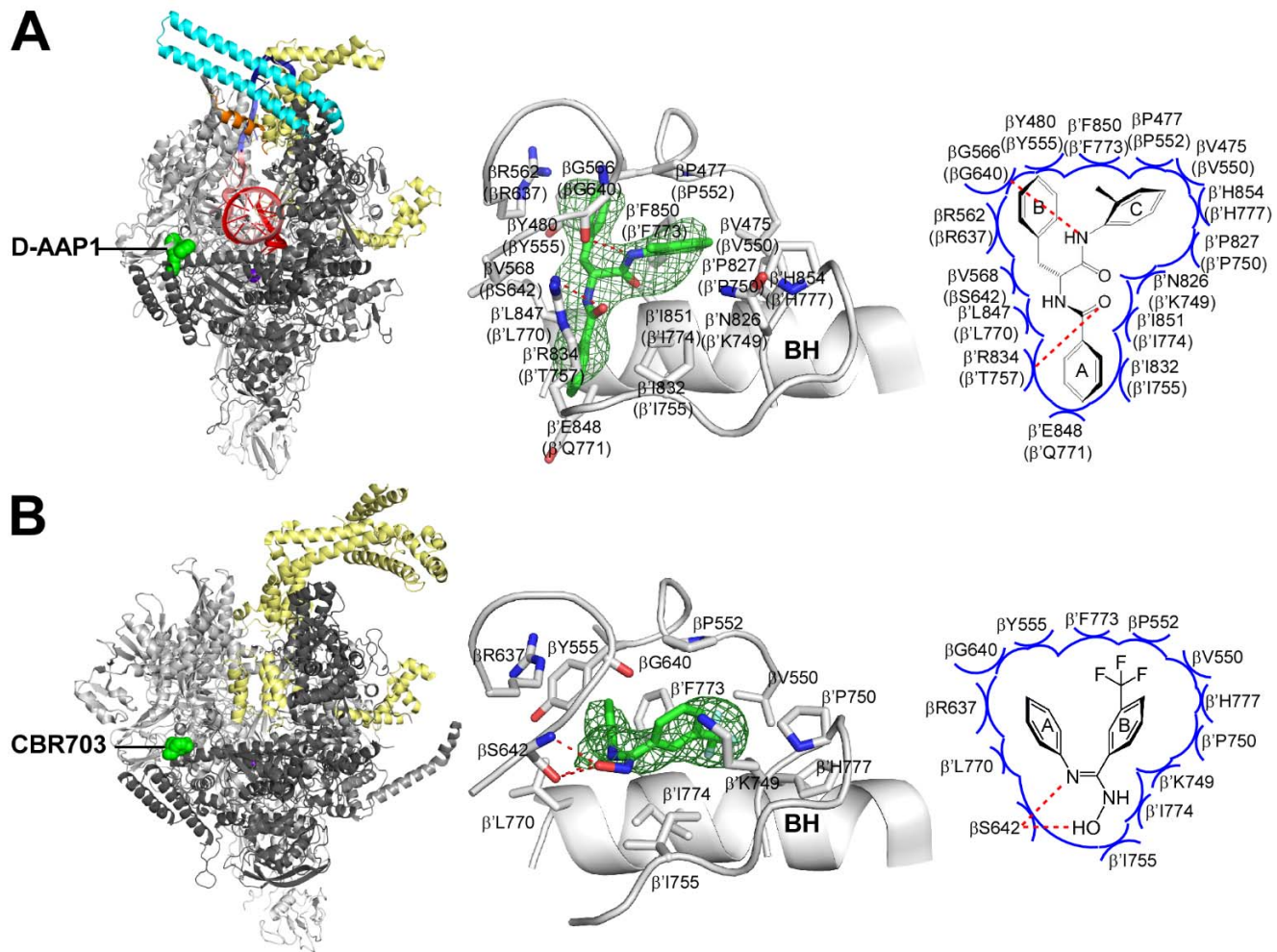


Figure S5

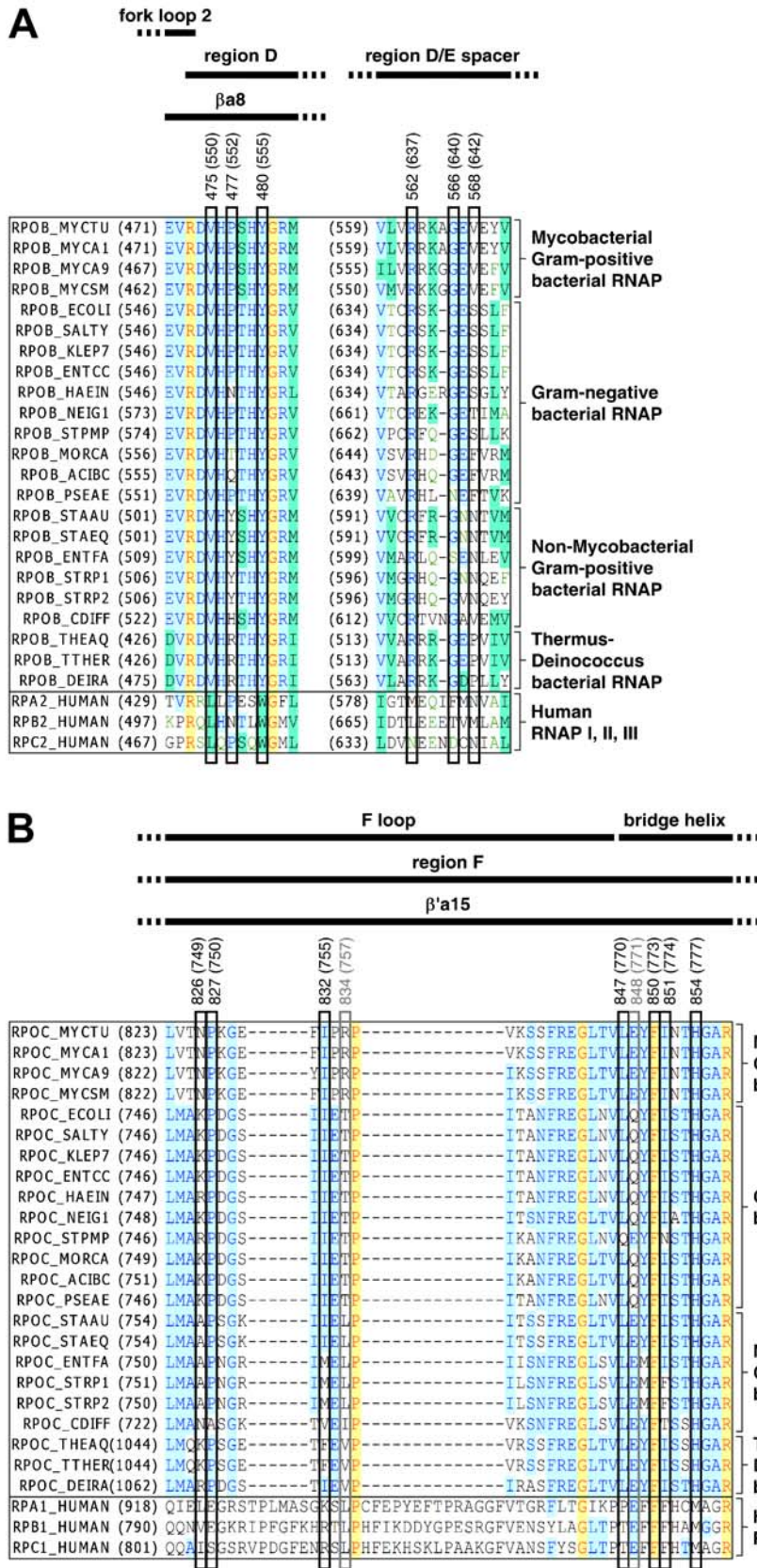


Figure S6